

1 **Energetic constraints on the pattern of changes to the hydrological cycle**  
2 **under global warming**

3 David B. Bonan,<sup>a</sup> Nicholas Siler,<sup>b</sup> Gerard H. Roe,<sup>c</sup> Kyle C. Armour,<sup>c</sup>

4 <sup>a</sup> *California Institute of Technology, Pasadena, California, USA*

5 <sup>b</sup> *Oregon State University, Corvallis, Oregon, USA*

6 <sup>c</sup> *University of Washington, Seattle, Washington, USA*

7 *Corresponding author:* David B. Bonan, [dbonan@caltech.edu](mailto:dbonan@caltech.edu)

8 ABSTRACT: The response of precipitation minus evaporation ( $P - E$ ) to global warming is inves-  
9 tigated using a moist energy balance model (MEBM) with a simple Hadley-Cell parameterization.  
10 The MEBM accurately emulates  $P - E$  changes simulated by a suite of global climate models  
11 (GCMs) under greenhouse-gas forcing. The MEBM also accounts for most of the intermodel  
12 differences in GCM  $P - E$  changes and better emulates GCM  $P - E$  changes when compared to  
13 the “wet-gets-wetter, dry-gets-drier” thermodynamic mechanism. The intermodel spread in  $P - E$   
14 changes are attributed to intermodel differences in radiative feedbacks, which account for 60–70%  
15 of the intermodel variance, with smaller contributions from radiative forcing and ocean heat uptake.  
16 Isolating the intermodel spread of feedbacks to specific regions shows that tropical feedbacks are  
17 the primary source of intermodel spread in  $P - E$  changes. The ability of the MEBM to emulate  
18 GCM  $P - E$  changes is further investigated using idealized feedback patterns. A less negative and  
19 narrowly peaked feedback pattern near the equator results in more atmospheric heating, which  
20 strengthens the Hadley Cell circulation in the deep tropics through an enhanced poleward heat  
21 flux. This pattern also increases gross moist stability, which weakens the subtropical Hadley Cell  
22 circulation. These two processes in unison increase  $P - E$  in the deep tropics, decrease  $P - E$  in the  
23 subtropics, and narrow the Intertropical Convergence Zone. Additionally, a feedback pattern that  
24 produces polar-amplified warming reduces the poleward moisture flux by weakening the merid-  
25 ional temperature gradient and the Clausius-Clapeyron relation. It is shown that changes to the  
26 Hadley Cell circulation and the poleward moisture flux are crucial for understanding the pattern of  
27 GCM  $P - E$  changes under warming.

28 SIGNIFICANCE STATEMENT: Changes to the hydrological cycle over the 21st century are  
29 predicted to impact ecosystems and socioeconomic activities throughout the world. While it is  
30 broadly expected that dry regions will get drier and wet regions will get wetter, the magnitude  
31 and spatial structure of these changes remains uncertain. In this study, we use an idealized  
32 climate model, which makes an assumption about how energy is transported in the atmosphere, to  
33 understand the processes setting the pattern of precipitation and evaporation under global warming.  
34 We first use the idealized climate model to explain why comprehensive climate models predict  
35 different changes to precipitation and evaporation across a range of latitudes. We show this  
36 arises primarily from climate feedbacks, which act to amplify or dampen the amount of warming.  
37 Ocean heat uptake and radiative forcing play secondary roles, but can account for a significant  
38 amount of the uncertainty in regions where ocean circulation influences the rate of warming. We  
39 further show that uncertainty in tropical feedbacks (mainly from clouds) affects changes to the  
40 hydrological cycle across a range of latitudes. We then show how the pattern of climate feedbacks  
41 affects how the patterns of precipitation and evaporation respond to climate change through a set of  
42 idealized experiments. These results show how the pattern of climate feedbacks impacts tropical  
43 hydrological changes by affecting the strength of the Hadley circulation and polar hydrological  
44 changes by affecting the transport of moisture to the high latitudes.

## 45 1. Introduction

46 The hydrological cycle, which describes the continuous movement of water on Earth, is a key  
47 component of the climate system. A fundamental measure of the hydrological cycle is the net  
48 water flux into the surface, which is equal to the difference between precipitation and evaporation  
49 ( $P - E$ ). The magnitude and spatial pattern of  $P - E$  affects the formation of water masses in the  
50 ocean (e.g., Schmitt et al. 1989; Large and Nurser 2001; Abernathy et al. 2016; Groeskamp et al.  
51 2019), the salinity and stratification of the ocean's mixed layer (e.g., de Boyer Montégut et al.  
52 2007), and the amount of runoff or availability of water over the land (e.g., Dai and Trenberth  
53 2002; Field and Barros 2014).  $P - E$  can also modulate transient climate change through changes  
54 in upper-ocean salinity, which impacts the degree of ocean heat uptake by changing the vertical  
55 stratification of the ocean (e.g., Liu et al. 2021). The magnitude and spatial pattern of  $P - E$  has  
56 been dramatically different in past climate states (e.g., Winguth et al. 2010; Boos 2012; Carmichael

57 et al. 2016; Burls and Fedorov 2017) and is predicted to change substantially over the next century  
 58 (e.g., Mitchell et al. 1987; Chou and Neelin 2004; Held and Soden 2006; Byrne and O’Gorman  
 59 2015; Siler et al. 2018).

60 In response to increased greenhouse-gas concentrations, state-of-the-art global climate models  
 61 (GCMs) consistently predict enhanced tropical precipitation and reduced subtropical precipitation,  
 62 particularly over the oceans. Held and Soden (2006) explained that this “wet-gets-wetter, dry-  
 63 gets-drier” paradigm can be understood by assuming that the change in  $P - E$  with warming is  
 64 due primarily to the change in moisture content of the atmosphere, with little contribution from  
 65 changes in atmospheric circulations. A simple scaling for these changes can be derived from the  
 66 fact that on climatological time scales,  $P - E$  is equal to the convergence of the mass-weighted,  
 67 vertically integrated moisture flux  $F_L$ :

$$P - E = -\nabla \cdot F_L. \quad (1)$$

68 As discussed in Held and Soden (2006) (hereafter referred to as HS06), the scaling arises by  
 69 assuming the change in  $F_L$  is dominated by the change in lower-tropospheric specific humidity,  
 70 with no changes in relative humidity and atmospheric circulation. These constraints mean that, as  
 71 the atmosphere warms,  $F_L$  will increase at close to the Clausius-Clapeyron rate, implying that:

$$F'_L \approx \alpha T' F_L, \quad (2)$$

72 where primes indicate the difference between the perturbed and control climates; and:

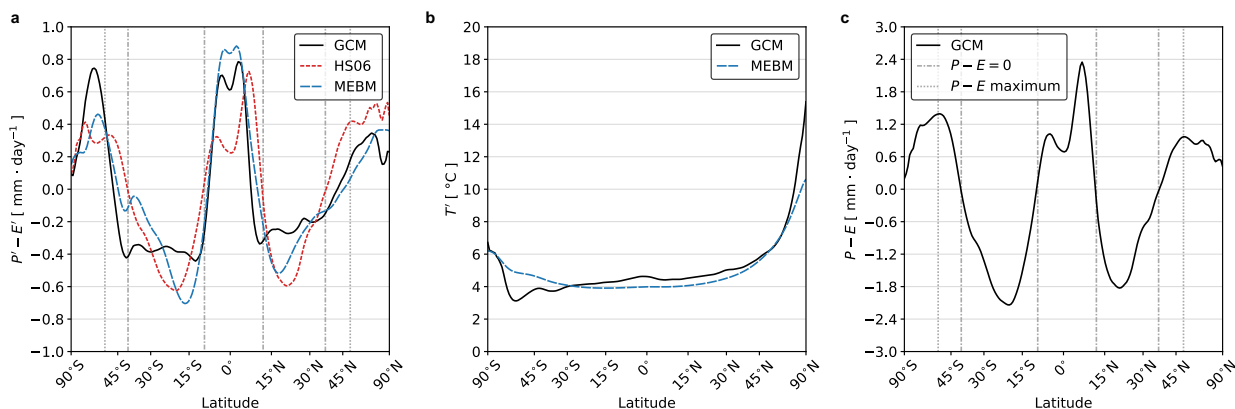
$$\alpha = \frac{L_v}{R_v T^2}, \quad (3)$$

73 is the Clausius-Clapeyron scaling factor, where  $L_v$  is the latent heat of vaporization ( $2.5 \times 10^6$   
 74 J kg<sup>-1</sup>),  $R_v$  is the gas constant of water vapor (461.5 J kg<sup>-1</sup> K<sup>-1</sup>), and  $T$  is the near-surface  
 75 air temperature. For typical atmospheric temperatures,  $\alpha$  ranges from around 6 % K<sup>-1</sup> (when  
 76  $T = 30^\circ\text{C}$ ) to more than 9 % K<sup>-1</sup> (when  $T = -30^\circ\text{C}$ ). If one assumes that gradients in  $\alpha$  and  $T'$  are  
 77 relatively small, Eq. (2) suggests that the change in  $P - E$  under warming will also scale at the

78 Clausius-Clapeyron rate, which results in:

$$P' - E' \approx \alpha T' (P - E). \quad (4)$$

79 Eq. (4) implies that a spatially uniform increase in precipitable water will enhance the existing  
 80 pattern of  $P - E$ : increasing  $P - E$  in the tropics and high latitudes and decreasing  $P - E$  in the  
 81 subtropics (e.g., Chou and Neelin 2004; Emori and Brown 2005; Held and Soden 2006; Seager  
 82 et al. 2010). Eq. (4) also implies that the climatological boundaries of where  $P - E = 0$  will remain  
 83 fixed.



84 **FIG. 1. Response of the hydrological cycle to global warming.** (a) The multi-model mean change in zonal-  
 85 mean precipitation minus evaporation ( $P' - E'$ ) from 20 CMIP5 simulations 126 – 150 years after an abrupt  
 86 quadrupling of  $\text{CO}_2$  relative to the pre-industrial average (black). The HS06 approximation (red dashed line) is  
 87 calculated from Eq. (4) and found by applying the multi-model zonal-mean change in near-surface air temperature  
 88 from the abrupt quadrupling of  $\text{CO}_2$  (black line in panel b) and the multi-model mean  $P - E$  climatology from  
 89 the preindustrial-control simulations (panel c) assuming  $\alpha = 7 \% \text{ K}^{-1}$  globally. The blue line shows the MEBM  
 90  $P' - E'$  pattern (which is described in Section 2). (b) The multi-model mean change in zonal-mean near-surface  
 91 air temperature ( $T'$ ) of (black) 20 CMIP5 GCMs and (blue line) the MEBM (see Section 2). (c) The multi-model  
 92 mean climatology of zonal-mean precipitation minus evaporation ( $P - E$ ) of 20 CMIP5 GCMs. The grey dashed  
 93 vertical lines in (a) and (c) represent the climatological  $P - E = 0$  in preindustrial-control simulations, which  
 94 corresponds to the subtropical regions; and the grey dotted vertical lines represent the climatological  $P - E$   
 95 maximum in preindustrial-control simulations, which is a measure of the storm track latitude.

96 HS06 found that Eq. (4) broadly captured the spatial structure of  $P' - E'$  as simulated by coupled  
97 GCMs under rising greenhouse-gas concentrations. Figure 1a shows the multi-model mean pattern  
98 of  $P' - E'$  averaged over years 126 – 150 after an abrupt quadrupling of  $\text{CO}_2$  ( $4 \times \text{CO}_2$ ) for 20 GCMs  
99 participating in phase 5 of the Coupled Model Intercomparison Project (CMIP5). Under global  
100 warming, GCMs show increasing  $P - E$  in the tropics and high latitudes and decreasing  $P - E$  in  
101 the subtropics (see black line in Fig. 1a). The red dashed line shows the HS06 approximation from  
102 Eq. (4) using the multi-model mean patterns of  $T'$  (Fig. 1b) and  $P - E$  (Fig. 1c) from the same  
103 20 GCMs, assuming that  $\alpha = 7\% \text{ K}^{-1}$  everywhere. While the approximation indeed captures the  
104 overall spatial pattern of  $P' - E'$  in GCM simulations of global warming, there are a few aspects  
105 that are not captured. Namely, Eq. (4) predicts  $P - E$  changes that are too large in the Northern  
106 Hemisphere extratropics and in the subtropical regions of both hemispheres, and predicts  $P - E$   
107 changes that are too small in the tropics and the Southern Hemisphere extratropics. Furthermore,  
108 Eq. (4) does not capture other robust features of  $P - E$  changes as seen in GCMs, such as the  
109 poleward expansion of the subtropics (defined by the boundary of where  $P - E = 0$ ; Lu et al.  
110 2007; Kang and Lu 2012), a poleward shift of the  $P - E$  maximum associated with the midlatitude  
111 storm tracks (Lu et al. 2010; Chang et al. 2012; Mbengue and Schneider 2013, 2017, 2018), and a  
112 contraction of the Inter-tropical Convergence Zone (ITCZ; Byrne and Schneider 2016b).

113 Some of the differences between the patterns of  $P' - E'$  predicted by Eq. (4) and simulated  
114 by GCMs have been reconciled through additional terms that account for the spatial pattern of  
115 temperature change or changing atmospheric circulations. For instance, Boos (2012) showed that  
116 including the pattern of temperature change is necessary for understanding  $P - E$  changes at the Last  
117 Glacial Maximum, where ice sheets greatly altered horizontal temperature gradients. Similarly,  
118 Byrne and O’Gorman (2015) showed that changes to the patterns of temperature and relative  
119 humidity are important when considering the response of  $P - E$  to warming over land, where  
120 warming is generally amplified and relative humidity generally decreases. Byrne and O’Gorman  
121 (2015) also noted that over land traditionally dry regions, such as deserts, may actually become  
122 wetter due to these additional terms. However, these modifications to the HS06 approximation  
123 are still fundamentally thermodynamic, and do not account for the potential impact of dynamical  
124 changes on the pattern of  $P - E$ . For example, the additional terms in Byrne and O’Gorman (2015)  
125 do not predict the increase in tropical  $P - E$  that GCMs suggest. Other studies have shown that

126 changing atmospheric circulations play an important role in determining the degree of subtropical  
127 expansion and narrowing of the ITCZ (Seager et al. 2010; Seager and Vecchi 2010), as well as  
128 poleward shifts in the mid-latitude storm tracks (Scheff and Frierson 2012).

129 More recently, Siler et al. (2018) simulated the change in zonal-mean  $P - E$  using a moist energy  
130 balance model (MEBM). The key physical processes in the MEBM is that it reflects the overall  
131 downgradient transport of moist-static energy in the atmosphere. The MEBM also includes a  
132 simple Hadley Cell parameterization, which transports latent energy diffusively down-gradient in  
133 the mid- to high-latitudes but allows for latent energy to travel up-gradient in the tropics. Siler et al.  
134 (2018) showed that the MEBM accurately emulates  $P - E$  changes as simulated by comprehensive  
135 CMIP5 GCMs under global warming and better emulates these changes when compared to the  
136 HS06 approximation (see blue dashed line in Fig. 1a). In particular, the MEBM correctly simulates  
137 the larger increase in  $P - E$  in the deep tropics and more muted  $P - E$  changes in the Northern  
138 Hemisphere extratropics (Fig. 1a). The MEBM also predicts the GCM expansion of the subtropics  
139 both equatorward and poleward, which can be seen in Fig. 1a as regions where  $P' - E' < 0$  extend  
140 across the dash-dot vertical lines (i.e.,  $P - E = 0$  in the climatology). Likewise, the dotted vertical  
141 lines in Fig. 1a denote the location of maximum  $P - E$  in the climatology, and a similar comparison  
142 with  $P' - E'$  shows that there is a poleward shift in the maximum  $P - E$ . Siler et al. (2018) argued  
143 that polar amplification — which is a robust feature of global warming — affects  $P' - E'$  by  
144 weakening the temperature dependence of the Clausius-Clapeyron relation and also decreasing  
145 the poleward moisture transport. This helps to explain why there is reduced high-latitude  $P - E$   
146 changes and why the subtropical regions expand under warming in the MEBM and GCMs, when  
147 compared to the HS06 approximation. However, it is still unclear why the pattern of  $P' - E'$  from  
148 the MEBM is in better agreement with GCMs than Eq. (4) in the deep tropics, capturing increasing  
149  $P - E$  in the deep tropics and a narrowing of the ITCZ region (Fig. 1a). Indeed, large-scale  
150 circulation features like the Hadley Cells dominate latent energy transport in the deep tropics.  
151 This leads to a key question: How important are changes to the strength of the Hadley Cells for  
152  $P - E$  changes in the tropics? Previous work (e.g., Byrne and Schneider 2016a,b) has shown that  
153 energetic arguments can be invoked to understand processes contributing to a narrowing of the  
154 ITCZ, but it remains unclear what energetic processes are driving these circulation changes and  
155 how these circulation changes relate to  $P - E$  changes. Other studies have also demonstrated that

156 Hadley Cell changes and ITCZ narrowing are likely related to radiative changes (Lau and Kim  
157 2015; Su et al. 2014, 2019), but there remains a gap in our understanding of how these energetic  
158 constraints impact  $P - E$  changes.

159 Better understanding processes that set the pattern of  $P' - E'$  may also help reduce uncertainty in  
160 future precipitation projections as sources of intermodel spread can be identified. Current GCMs  
161 exhibit a large intermodel spread in the pattern of  $P' - E'$  under global warming, and the exact  
162 reason for this spread remains unknown (Prein and Pendergrass 2019). Previous studies have  
163 shown that tropical radiative feedbacks contribute to uncertainty in the amount of warming that is  
164 nearly spatially uniform, while polar radiative feedbacks contribute to uncertainty in the amount  
165 of warming that is confined to the poles (Roe et al. 2015; Bonan et al. 2018). Yet, an important  
166 question remains unanswered: What processes constitute the greatest sources of uncertainty in the  
167 pattern of  $P' - E'$  under climate change? The ability of the MEBM to emulate the pattern of  $P' - E'$   
168 simulated by GCMs under greenhouse-gas forcing (see Fig. 1a) suggests the MEBM can also be  
169 used to examine drivers of uncertainty in  $P' - E'$ .

170 In this paper, we have two specific aims:

- 171 1. We identify sources of intermodel spread in the pattern of  $P' - E'$  under global warming.  
172 To do this, we first show that the MEBM is able to account for a majority of the intermodel  
173 variance in  $P' - E'$  across a range of latitudes for GCMs under  $4 \times \text{CO}_2$ . We then link the  
174 intermodel spread in  $P' - E'$  to radiative feedbacks, radiative forcing, and ocean heat uptake.
- 175 2. We further investigate differences between the simple thermodynamic perspective introduced  
176 by HS06 and the downgradient energy transport perspective introduced by Siler et al. (2018).  
177 Specifically, we use the MEBM to consider how the pattern of radiative feedbacks impacts the  
178 pattern of  $P' - E'$  in the tropics and extratropics. We show that changes to the net heating of the  
179 atmosphere and gross moist stability act to strengthen and weaken the Hadley Cell in different  
180 regions, which alters moisture transport to the tropics, narrows the ITCZ and increases  $P - E$   
181 in the deep tropics. We also show how changes in the meridional temperature gradient alters  
182 poleward moisture transport.

183 The paper is structured as follows. In Section 2, we describe the MEBM and Hadley Cell  
184 parameterization. In Section 3, we assess the skill of the MEBM in emulating GCMs under  
185 greenhouse-gas forcing and use the MEBM to identify sources of uncertainty in the pattern of

186  $P' - E'$ . In Section 4, we examine how the pattern of radiative feedbacks impacts  $P - E$  changes in  
 187 the deep tropics and extratropics using a set of simple scalings and compare these results to output  
 188 from CMIP5 GCMs. Finally, in Section 5, we discuss key results and implications of this work.

## 189 2. A modified moist energy balance model

190 A series of studies have shown that downgradient energy transport by the atmosphere is remark-  
 191 ably successful at emulating the zonal-mean climate, and its response to greenhouse-gas forcing  
 192 (Flannery 1984; Hwang and Frierson 2010; Roe et al. 2015; Siler et al. 2018; Bonan et al. 2018;  
 193 Merlis and Henry 2018; Armour et al. 2019; Russotto and Biasutti 2020; Lutsko et al. 2020; Hill  
 194 et al. 2022; Beer and Eisenman 2022). When applied to climate change, the MEBM assumes that  
 195 the anomalous northward column-integrated atmospheric energy transport  $F'(x)$  is proportional  
 196 to the meridional gradient of anomalous near-surface moist static energy  $h' = c_p T' + L_v q'$ , which  
 197 gives:

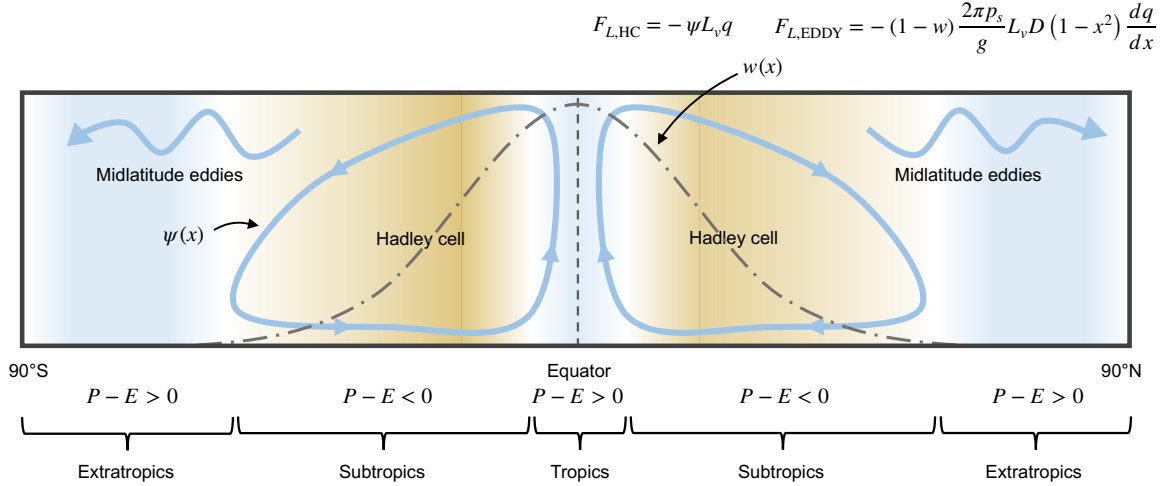
$$F'(x) = \frac{2\pi p_s}{g} D (1 - x^2) \frac{dh'}{dx}, \quad (5)$$

198 where  $c_p$  is the specific heat of air ( $1005 \text{ J kg}^{-1} \text{ K}^{-1}$ ),  $q'$  is the anomalous near-surface specific  
 199 humidity (assuming fixed relative humidity of 80%),  $p_s$  is surface air pressure (1000 hPa),  $g$  is  
 200 the acceleration due to gravity ( $9.81 \text{ m s}^{-2}$ ),  $D$  is a constant diffusion coefficient (with units of  $\text{m}^2$   
 201  $\text{s}^{-1}$ ),  $x$  is sine latitude, and  $1 - x^2$  accounts for the spherical geometry.

202 Under warming, the anomalous heating of the atmosphere must be balanced by the divergence  
 203 of  $F'(x)$ . We define  $R_f(x)$  as the local top-of-atmosphere (TOA) radiative forcing;  $\lambda(x)$  as the  
 204 local radiative feedback, defined as the change in net upward TOA radiative flux per degree of  
 205 local surface warming ( $\text{W m}^{-2} \text{ K}^{-1}$ ); and  $G'(x)$  as the change in net surface heat flux, which is  
 206 equivalent to the divergence of ocean heat transport and ocean heat storage. Combining these three  
 207 terms (i.e., the anomalous heating of the atmosphere) with the divergence of Eq. (5) gives:

$$R_f(x) - G'(x) + \lambda(x)T'(x) = \nabla \cdot F'(x), \quad (6)$$

208 which is a single differential equation that can be solved numerically for  $T'(x)$  and  $F'(x)$  given  
 209 patterns of  $R_f(x)$ ,  $G'(x)$ , and  $\lambda(x)$  and a value of  $D$ .



210 **FIG. 2. Schematic depicting the Hadley Cell parameterization in the moist energy balance model.** A  
 211 Gaussian weighting function  $w(x)$ , shown in the grey dash-dot line is used to partition atmospheric heat transport  
 212  $F(x)$  into a component due to the Hadley Cell  $F_{HC}(x)$  and a component due to eddies  $F_{EDDY}(x)$ . A streamfunction  
 213  $\psi$  is then approximated using assumptions about gross moist stability (see Section 2 and Appendix B).  $\psi$  is then  
 214 used to flux moisture back up the meridional moist-static energy gradient while the rest is diffused down the  
 215 meridional moist-static energy gradient and modulated by the weighting function. By summing the two terms  
 216 and taking the divergence, a pattern of  $P - E$  is obtained.

217 To simulate a realistic hydrological cycle, we follow Siler et al. (2018) and Armour et al.  
 218 (2019) and define a Gaussian weighting function  $w(x)$  that partitions the transport of anomalous  
 219 latent and dry-static energy within the tropics. A schematic depicting the mean-state Hadley Cell  
 220 parameterization is shown in Figure 2. Following Siler et al. (2018), we divide  $F'(x)$  into a  
 221 component due to the Hadley Cells  $F'_{HC}(x)$  and a component due to the eddies  $F'_{EDDY}(x)$ , and  
 222 define  $w(x)$  as the fraction of total energy transport that is accomplished by the Hadley Cells at a  
 223 given latitude:

$$F'_{HC}(x) = w(x)F'(x) \text{ and } F'_{EDDY}(x) = (1 - w(x))F'(x), \quad (7)$$

224 and

$$w(x) = \exp\left(\frac{-x^2}{\sigma_x^2}\right), \quad (8)$$

225 where  $\sigma_x$  is a width parameter, which we set to 0.30 following Siler et al. (2018). In this formulation,  
 226 eddies account for essentially all anomalous energy transport poleward of 45°S and 45°N, while  
 227 the Hadley Cell accounts for most anomalous energy transport between 10°S and 10°N. In this  
 228 way, the overall downgradient transport of  $h'$  is maintained, but latent energy is properly routed  
 229 with a fixed  $w$ . Note that this formulation explicitly leaves out representation of the extratropical  
 230 components of the mean meridional circulation (i.e., Ferrel and polar cells) and does not allow for  
 231 the extent of the Hadley Cell to change under warming.

232 In the mean-state climate, poleward atmospheric heat transport by the Hadley Cell  $F_{\text{HC}}(x)$  is  
 233 equal to:

$$F_{\text{HC}}(x) = \psi(x)H(x), \quad (9)$$

234 where  $\psi(x)$  is the mass transport ( $\text{kg s}^{-1}$ ) in each branch of the Hadley Cell and  $H(x)$  is the gross  
 235 moist stability, defined as the difference between  $h$  in the upper and lower branches at each latitude  
 236 (see details below). However, because we are considering  $P - E$  changes under warming, the  
 237 anomalous poleward atmospheric heat transport by the Hadley Cell can be represented as:

$$F'_{\text{HC}}(x) = \psi'(x)\overline{H}(x) + \overline{\psi}(x)H'(x) + \psi'(x)H'(x), \quad (10)$$

238 where  $\psi'(x)$  is the anomalous mass transport ( $\text{kg s}^{-1}$ ) in each branch of the Hadley Cell and  
 239  $H'(x)$  is the anomalous gross moist stability (i.e., the difference between  $h'$  in the upper and lower  
 240 branches at each latitude). Note that we have written Eq. (10) in terms of a perturbation around the  
 241 climatological mean-state. Appendix B details how the climatological state is approximated using  
 242 the MEBM. In Section 3, we use the climatological state of each GCM. For the idealized analyses  
 243 of Section 4, the climatological state is equivalent to the multi-model mean climatological state of  
 244 the 20 CMIP5 GCMs under preindustrial conditions, but symmetric about the equator so as not to  
 245 introduce hemispheric asymmetries.

246 Following Held (2001), we assume that anomalous upper tropospheric moist-static energy is  
 247 uniform in the tropics with a constant value of  $h'_0$ . Thus, variations in  $H'(x)$  are due entirely to  
 248 meridional variations in  $h'$  giving  $H'(x) \approx h'_0 - h'(x)$ , where  $h'_0 = 1.08 \times h'(0)$ , or 8% above  $h'$  at  
 249 the equator ( $x = 0$ ). Note that this value is slightly higher than the value used by Siler et al. (2018),  
 250 which is 6% above  $h'$  at the equator, but was found to better emulate  $P' - E'$  in GCMs. Each GCM

251 uses the same scaling factor. Higher scaling factors result in weaker Hadley Cell mass fluxes and  
 252 less tropical  $P - E$ . The anomalous latent energy transport by the Hadley Cell  $F'_{L,HC}(x)$  is thus:

$$F'_{L,HC}(x) = -\left(\psi'(x)L_v\bar{q}(x) + \bar{\psi}(x)L_vq'(x) + \psi'(x)L_vq'(x)\right). \quad (11)$$

253 The assumption about moisture transport holds because the upper branch of the Hadley Cell is  
 254 essentially dry, meaning anomalous latent energy transport is confined to the lower branch. With  
 255 this simple Hadley Cell parameterization, the anomalous latent energy transport can be obtained  
 256 by summing the terms due to the Hadley Cells and eddies:

$$F'_L(x) = F'_{L,HC}(x) + F'_{L,EDDY}(x). \quad (12)$$

257 The divergence of  $F'_L(x)$  (Eq. 12) then yields the change in  $P - E$ :

$$P' - E' = -\nabla \cdot F'_L(x) = -\frac{1}{2\pi a^2} \frac{dF'_L}{dx}. \quad (13)$$

258 The essential feature of the MEBM framework is that it allows for a self-consistent representation  
 259 of atmospheric heat transport, while allowing us to examine how different factors, such as the  
 260 patterns of  $\lambda$ ,  $G'$ ,  $R_f$ , and  $T'$  impact that pattern of  $P' - E'$ . It also important to note this framework  
 261 ensures that  $P' = E'$  globally.

### 262 3. Changes to the hydrological cycle in a moist energy balance model

271 We first assess the ability of the MEBM to emulate a suite of comprehensive GCMs under  
 272 greenhouse-gas forcing largely following Siler et al. (2018). To do this, we compute the model-  
 273 specific patterns of  $R_f$ ,  $G'$ , and  $\lambda$  from 20 different CMIP5 GCMs (see Appendix A) and calculate  
 274 the  $P' - E'$  pattern from the MEBM defined in Section 2. Note, for this section we use model-  
 275 specific values of  $D$  and climatological states from a climatological version of the MEBM (see  
 276 Appendix B).

277 Figure 3 shows the pattern of  $P' - E'$  from each GCM, the MEBM solution, and the HS06  
 278 approximation. While the overall pattern of “wet-gets-wetter, dry-gets-drier” is similar across  
 279 both the HS06 approximation and MEBM, there is much better agreement between GCMs and

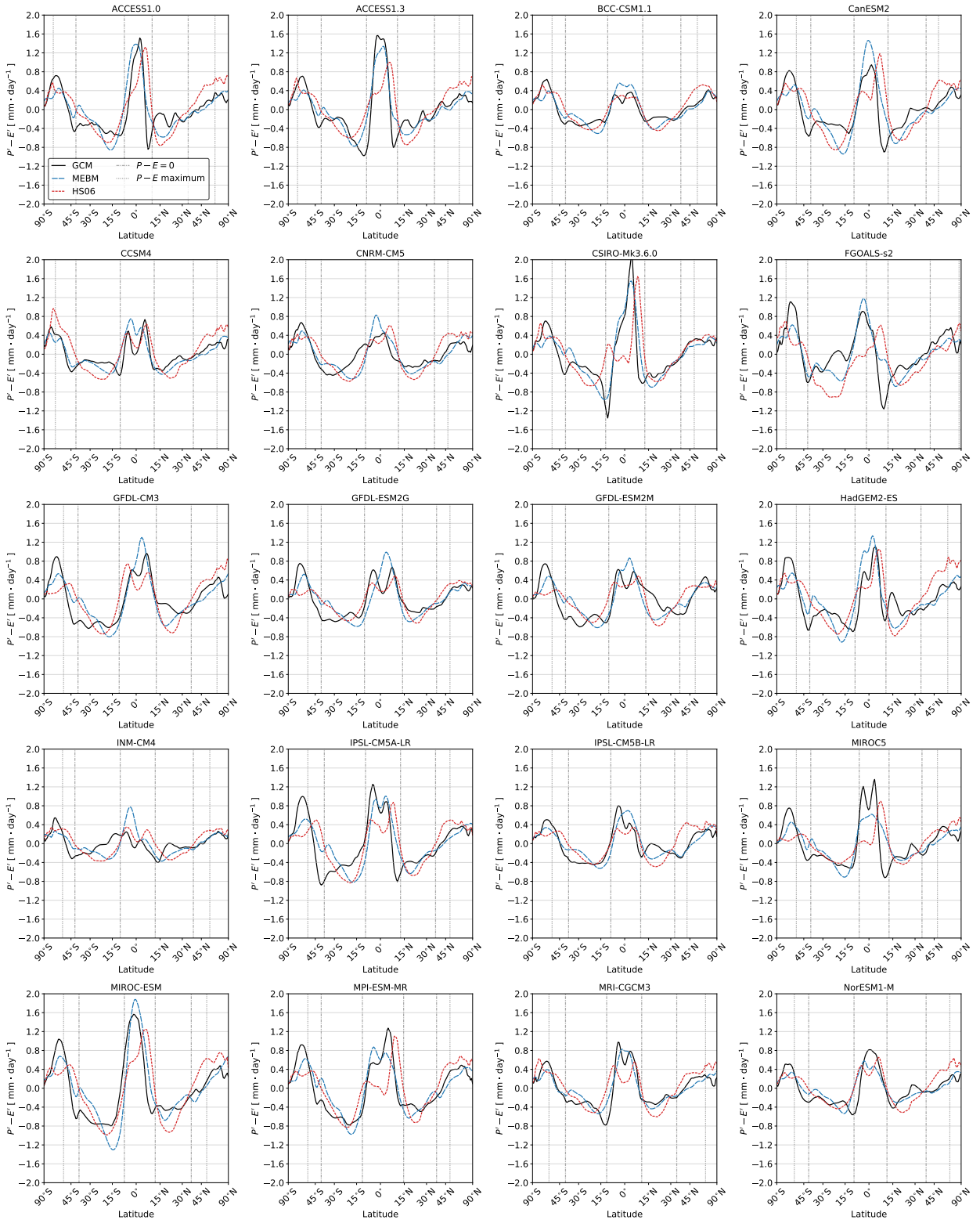
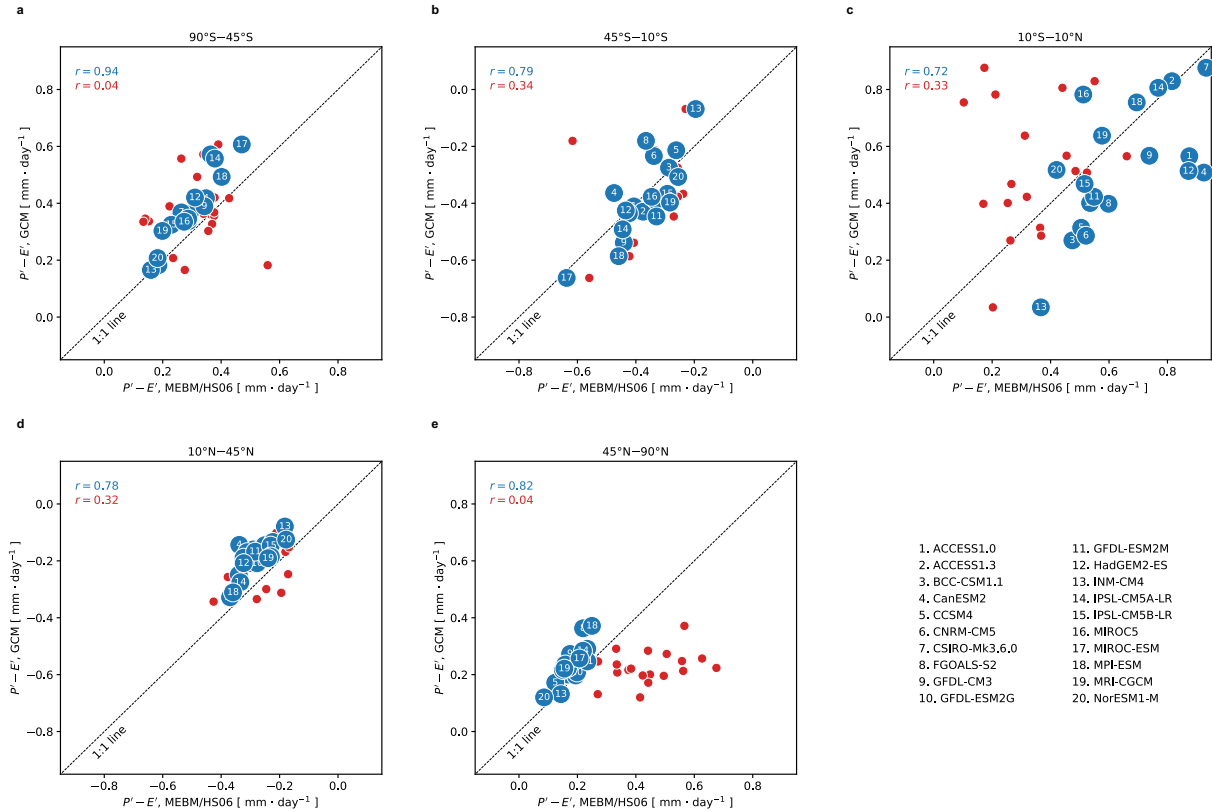


Fig. 3. See next page.

263 **FIG. 3. Response of the hydrological cycle to global warming in a moist energy balance model.** The  
 264 pattern of  $P' - E'$  in 20 CMIP5 simulations 126 – 150 years after an abrupt quadrupling of  $\text{CO}_2$ . The black line  
 265 denotes the GCM, the blue line denotes the MEBM solution, and the red line denotes the HS06 approximation.  
 266 The grey line denotes an individual GCM or simulation and the colored line denotes the multi-model mean. The  
 267 grey dashed vertical lines in (a) and (c) represent the  $P - E = 0$  boundary in the climatology, which corresponds  
 268 to the subtropical regions; and the grey dotted vertical lines represent the  $P - E$  maximum, which is a measure  
 269 of the latitude of the storm tracks. Changes in subtropical boundaries and stormtrack latitude can be inferred by  
 270 comparing the  $P' - E'$  changes with these vertical lines.

280 the MEBM than between GCMs and the HS06 approximation. For example, in GCMs with large  
 281 values of  $P' - E'$  in the deep tropics (e.g., ACCESS-1.0, CanESM2, CSIRO-Mk3.6.0, and MIROC-  
 282 ESM) there is a good agreement between the MEBM and GCMs that is not captured by the HS06  
 283 approximation, suggesting that the MEBM is capturing changes in latent energy transport that the  
 284 HS06 approximation leaves out. The MEBM also captures a narrowing of the ITCZ region, which  
 285 occurs in every GCM analyzed here, and can be inferred from Fig. 3 because  $P' - E'$  is negative  
 286 at the equatorward climatological  $P - E = 0$  line (dash-dot line in each panel). In the extratropical  
 287 regions, the MEBM captures, better than the HS06 approximation, the more muted  $P - E$  changes  
 288 also shown by GCMs (e.g., ACCESS-1.3, CCSM4, HadGEM2-ES). The MEBM also broadly  
 289 captures the expansion of the subtropical regions in each GCM.

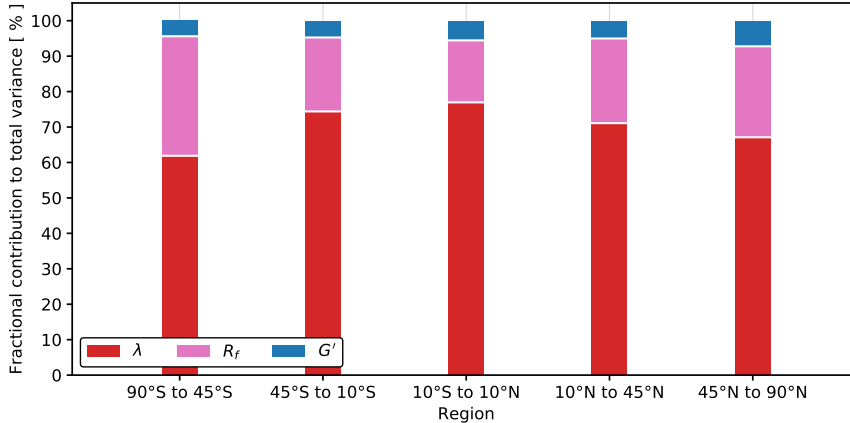
294 To quantitatively compare the pattern of  $P' - E'$  from each individual GCM, the MEBM solution,  
 295 and the HS06 approximation, we take area-weighted averages of  $P' - E'$  in five distinct regions  
 296 that represent the extratropical regions ( $90^\circ\text{S}$  to  $45^\circ\text{S}$  and  $45^\circ\text{N}$  to  $90^\circ\text{N}$ ), the subtropics ( $45^\circ\text{S}$   
 297 to  $10^\circ\text{S}$  and  $10^\circ\text{N}$  to  $45^\circ\text{N}$ ) and the deep tropics ( $10^\circ\text{S}$  to  $10^\circ\text{N}$ ). In the extratropical regions, the  
 298 MEBM accounts for approximately 70% of the intermodel variance while the HS06 approximation  
 299 accounts for none (Fig. 4a and 4e). In the subtropics, the MEBM accounts for less intermodel  
 300 variance ( $r^2 \approx 0.60$ ; Fig. 4b and 4d), but still far more than the HS06 approximation ( $r^2 \approx 0.10$ ). In  
 301 the deep tropics, where the MEBM solution predicts larger increases in  $P - E$  when compared to  
 302 the HS06 approximation, the MEBM accounts for approximately 50% of the intermodel variance,  
 303 compared with about 10% for the HS06 approximation (Fig. 4c).



290 **FIG. 4. Skill of the moist energy balance model.** Scatter plots of the area-averaged  $P' - E'$  in the GCM, Held  
 291 and Soden (2006) approximation (red), and MEBM (blue) from (a) 90°S to 45°S, (b) 45°S to 10°S, (c) 10°S to  
 292 10°N, (d) 10°N to 45°N, and (e) 45°N to 90°N. The top left corner of each plot shows the Pearson correlation  
 293 coefficient between the  $P' - E'$  responses from the MEBM and GCM (blue) and HS06 and GCM (red).

304 *a. Sources of uncertainty*

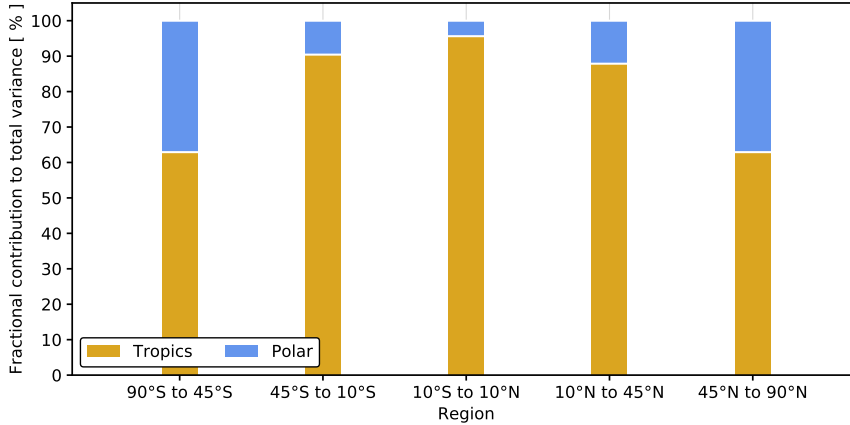
308 Having demonstrated that the MEBM emulates the pattern of  $P' - E'$  for each individual GCM,  
 309 we next investigate the reason for the good agreement between the MEBM and GCMs, and the  
 310 intermodel spread of these  $P' - E'$  patterns. Uncertainty in the MEBM mainly arises from three  
 311 sources: radiative forcing  $R_f$ , ocean heat uptake  $G'$ , and radiative feedbacks  $\lambda$ . Following Bonan  
 312 et al. (2018), we disaggregate the  $P' - E'$  patterns into separate contributions from  $R_f$ ,  $G'$ , and  $\lambda$   
 313 by creating a baseline pattern of  $P' - E'$  for the MEBM using the multi-model mean patterns of  
 314  $R_f$ ,  $G'$ , and  $\lambda$ . We then run the MEBM using the GCM-specific patterns of either  $R_f$ ,  $G'$ , and  $\lambda$   
 315 (Figure A1) while holding the other two variables fixed at their multi-model mean patterns. This  
 316 generates a spread of MEBM  $P' - E'$  patterns due to intermodel differences in either  $R_f$ ,  $G'$ , and



305 FIG. 5. Sources of uncertainty in the response of the hydrological cycle to global warming in different  
 306 regions. Fractional contribution of  $\lambda$ ,  $R_f$ , and  $G'$  to the total variance in  $P' - E'$  for averages from 90°S to 45°S,  
 307 45°S to 10°S, 10°S to 10°N, 10°N to 45°N, and 45°N to 90°N.

317  $\lambda$ . To understand the relative importance of each contributing factor, we calculate the variance  
 318 of  $P' - E'$  as a function of latitude from each individual factor. We then compute the fractional  
 319 contribution of each factor to the total variance by assuming that the variance associated with each  
 320 factor can be added linearly.

321 Figure 5 shows the fractional contribution of  $R_f$ ,  $G'$ , and  $\lambda$  to the total variance in  $P' - E'$  for  
 322 the same regions described above. Across all regions intermodel variations in  $\lambda$  are the leading  
 323 cause of intermodel variations in  $P' - E'$ , accounting for 60 – 75% of the intermodel variance.  
 324 In the extratropical regions, the contribution of  $\lambda$  to the intermodel spread in  $P' - E'$  is smaller  
 325 than in the tropics (Fig. 5).  $R_f$  accounts for 15 – 30% of the intermodel variance in  $P' - E'$   
 326 patterns, and accounts for more intermodel variance in the extratropical regions when compared  
 327 to the tropics. Intermodel variations in  $G'$  account for 5 – 8% of the intermodel variance across all  
 328 regions. Note that these averages represent broad swaths of  $P' - E'$ , which exhibits large spatial  
 329 variations as a function of latitude. The same analysis as a continuous function of latitude yields a  
 330 greater influence of  $G'$  at some latitudes, accounting for approximately 30 – 40% of the intermodel  
 331 variance in  $P' - E'$  in regions of large ocean heat uptake, such as the North Atlantic and Southern  
 332 Ocean (Marshall et al. 2015).



334 **FIG. 6. Local and remote influence of regional climate feedbacks on the response of the hydrological**  
 335 **cycle to global warming.** Fractional contribution of intermodel variations of  $\lambda$  in the tropical (30°S to 30°N)  
 336 and extratropical regions (90°S to 30°S and 30°N to 90°N) to the total variance in  $P' - E'$  for averages from 90°S  
 337 to 45°S, 45°S to 10°S, 10°S to 10°N, 10°N to 45°N, and 45°N to 90°N.

333 *b. Local and remote impacts of climate feedbacks*

338 Given that the intermodel spread of  $\lambda$  is the main source of uncertainty in the pattern of  $P' - E'$ , we  
 339 next consider the relative importance of  $\lambda$  in different regions. The remote-versus-local influence  
 340 of  $\lambda$  has been shown to be an important factor when considering uncertainty in the pattern of  
 341 temperature (Roe et al. 2015; Bonan et al. 2018), but its influence on changes to  $P' - E'$  is less  
 342 understood. To examine this, we run the MEBM with the multi-model mean patterns of  $R_f$  and  
 343  $G'$ , and confine the intermodel spread of  $\lambda$  to the tropics (30°S to 30°N) and extratropics (90°S to  
 344 30°S and 30°N to 90°N) while the other region is set to the multi-model mean of  $\lambda$ . This isolates  
 345 the impact of uncertainty in one region on  $P' - E'$  uncertainty in other regions, but does not isolate  
 346 inter-hemispheric changes. Note that these regions span equal areas of the globe.

347 Figure 6 shows the fractional contribution of intermodel variations of  $\lambda$  in the tropical and  
 348 extratropical regions to the total variance in  $P' - E'$  for the same regions examined above. In the  
 349 deep tropics and subtropics, intermodel differences in tropical  $\lambda$  account for 85-92% of intermodel  
 350 variance in  $P' - E'$ . In the extratropical regions, intermodel differences in tropical  $\lambda$  contribute  
 351 to approximately 60% of the intermodel variance in  $P' - E'$ . Notably, intermodel variations in  $\lambda$   
 352 in the extratropical regions contribute little to intermodel variations in  $P' - E'$  in the deep tropics  
 353 and subtropics, but contribute approximately 40% of the intermodel variations of  $P - E$  in the

354 extratropical regions. This is similar to the results of Bonan et al. (2018), where tropical-feedback  
355 uncertainty was found to contribute to warming uncertainty that was nearly uniform with latitude.

#### 356 **4. Impact of radiative feedback patterns on hydrological changes**

357 Having shown that the MEBM emulates the pattern of  $P' - E'$  simulated by GCMs under  
358 greenhouse-gas forcing with high skill, and that this pattern is largely determined by radiative  
359 feedbacks, we now use the MEBM with idealized radiative-feedback patterns and a set of simple  
360 scalings to investigate the specific mechanisms responsible for setting the  $P' - E'$  pattern. The  
361 radiative-feedback patterns are constructed to illustrate key differences between the MEBM and  
362 HS06 approximation. Note that the pattern of  $P' - E'$  from the HS06 approximation is purely  
363 thermodynamic, arising from the climatological pattern of  $P - E$  and the spatial pattern of warming,  
364 whereas the pattern of  $P' - E'$  from the MEBM is both thermodynamic and dynamic, arising from  
365 changes in latent energy transport from eddies and the Hadley Cells, both of which are constrained  
366 by the overall energetic demand in the atmosphere.

##### 367 *a. Experiments and overview*

378 Because we showed that the pattern of radiative feedbacks contributes most to the intermodel  
379 spread of  $P' - E'$ , we first set  $G'(x) = 1.54 \text{ W m}^{-2}$  and  $R_f(x) = 6.35 \text{ W m}^{-2}$ , which are the multi-  
380 model and global-mean values of the CMIP5 GCMs.  $D$  is set to  $1.05 \times 10^6 \text{ m}^2 \text{ s}^{-1}$ , which is the  
381 multi-model mean value of the CMIP5 GCMs. We also take the multi-model mean climatological  
382 MEBM variables ( $\psi$ ,  $H$ ,  $T$ ) and make them symmetric about the equator. Thus, any asymmetries  
383 in the analyses of Section 4 result from asymmetries in the pattern of radiative feedbacks only.  
384 Next, we create four  $\lambda$  patterns that broadly represent the intermodel spread of CMIP5 GCMs (see  
385 Figure A1) and produce four distinct patterns of warming (Fig. 7). These patterns are as follows:

- 386 1. The first  $\lambda$  pattern is weakly negative in the deep tropics, positive in the subtropics, and  
387 negative in the extratropics (Fig. 7a). This  $\lambda$  pattern produces a pattern of warming that is  
388 uniform with latitude and equivalent to the multi-model and global-mean value of warming  
389 from the CMIP5 GCMs. This pattern was calculated by prescribing a uniform  $T'$  in Eq. (6)  
390 and solving for  $\lambda$ .

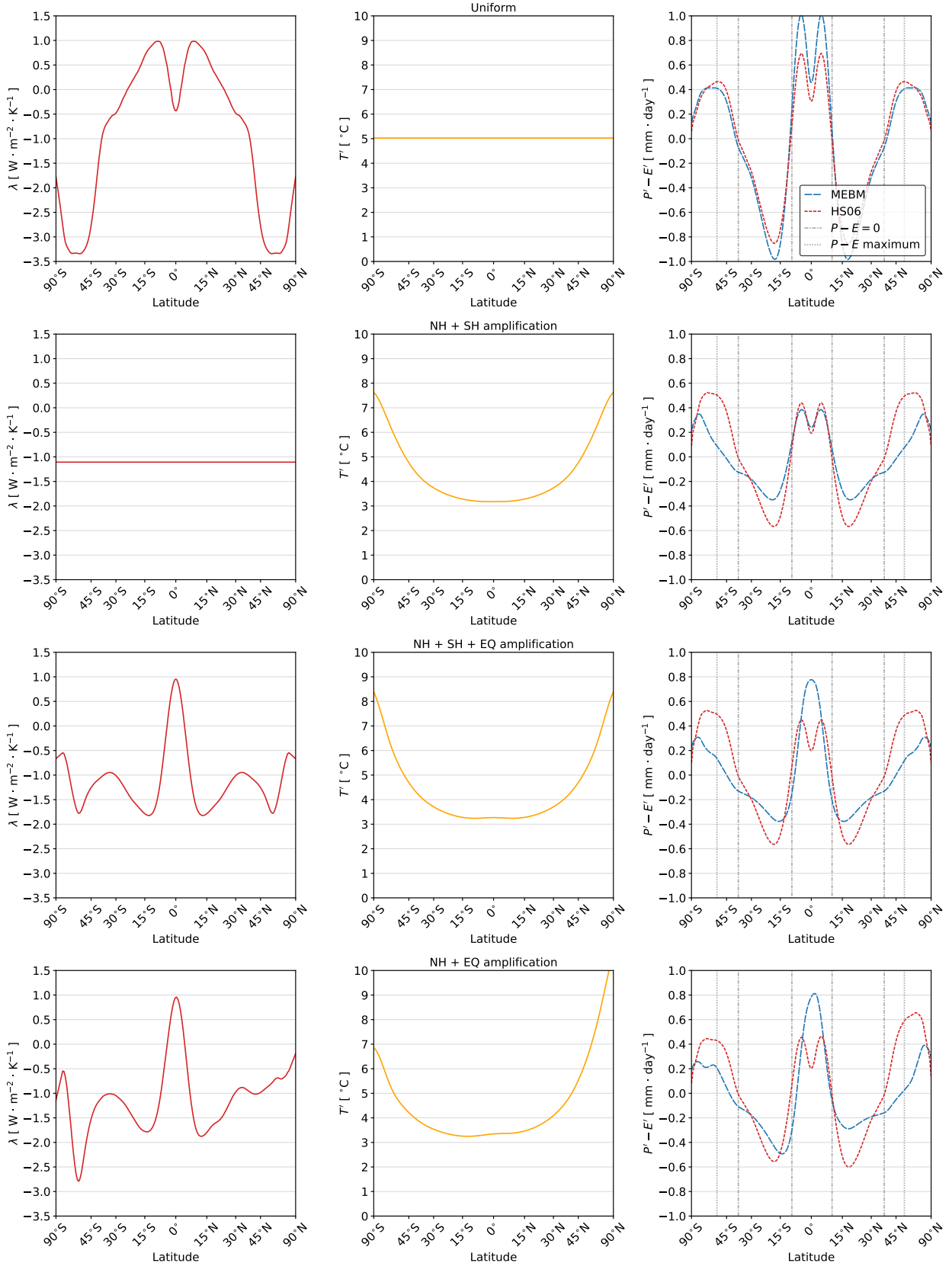


FIG. 7. See next page.

368 **FIG. 7. Impact of radiative feedback patterns on the response of the hydrological to global warming.** A  
 369 (left) pattern of the net radiative feedback that induces a (middle) pattern of warming; (a) that is uniform; (b)  
 370 with equal degrees of polar amplification in the Northern Hemisphere and Southern Hemisphere; (c) with equal  
 371 degrees of polar amplification in the Northern Hemisphere and Southern Hemisphere and amplified warming  
 372 on the equator; and (d) with more polar amplification in the Northern Hemisphere than Southern Hemisphere  
 373 and amplified warming on the equator. The right panel shows the pattern of  $P' - E'$  for each pattern of the  
 374 net radiative feedback. The blue dashed line denotes the MEBM solution and the red dashed line is the Held  
 375 and Soden (2006) approximation assuming  $\alpha = \% K^{-1}$  globally and using the multi-model mean climatological  
 376 pattern of  $P - E$  from 20 preindustrial control simulations, which is shown in Fig. 1c. Note that the climatological  
 377 patterns have been symmetrized about the equator.

- 391 2. The second  $\lambda$  pattern is uniform with latitude and equivalent to the multi-model and global-  
 392 mean value of  $\lambda$  from the CMIP5 GCMs (Fig. 7b). This  $\lambda$  pattern produces a pattern of  
 393 warming that is polar-amplified in both hemispheres and contains little-to-no structure in the  
 394 deep tropics.
- 395 3. The third  $\lambda$  pattern is symmetric across both hemispheres but contains a narrowly positive  
 396 peak value of  $\lambda$  in the deep tropics and negative values elsewhere (Fig. 7c). This pattern  
 397 was calculated by taking the pattern of  $\lambda$  from CSIRO-Mk3.6.0, which exhibits the largest  
 398 increases in  $P - E$  in the deep tropics, and making it symmetric across the equator. This  $\lambda$   
 399 pattern produces a pattern of warming that is also polar-amplified in both hemispheres, but  
 400 contains a slight amplification of warming near the equator.
- 401 4. The fourth  $\lambda$  pattern is antisymmetric across both hemispheres but still contains a narrowly  
 402 positive peak value of  $\lambda$  in the deep tropics and negative values elsewhere (Fig. 7d). This  
 403  $\lambda$  pattern is from CSIRO-Mk3.6.0 and produces a pattern of warming that is more polar-  
 404 amplified in the Arctic and less polar-amplified in the Antarctic, but also contains a slight  
 405 amplification of warming near the equator.

406 The resulting patterns of  $P' - E'$  are shown in the right columns of Figure 7, along with a  
 407 comparison to the HS06 approximation. We briefly describe the patterns, before analyzing the  
 408 causes in the next two subsections, focusing separately on the tropics and extratropics. For Pattern  
 409 1, when  $\lambda$  is mostly positive in the subtropics and negative in the extratropics (Fig. 7a), the

410 pattern of warming is uniform. This results in a  $P' - E'$  pattern that is nearly identical to the HS06  
411 approximation (i.e., Eq. 4), with increasing  $P - E$  in the tropics and high-latitudes and decreasing  
412  $P - E$  in the subtropics. Note that this  $P - E$  pattern contains no change in the subtropical boundaries  
413 or narrowing of the ITCZ. However, for Pattern 2, when  $\lambda$  is uniform with latitude, there is a polar-  
414 amplified pattern of warming, which results in a pattern of  $P' - E'$  that is different between the  
415 MEBM and HS06. For polar-amplified warming, while the pattern of  $P' - E'$  for the MEBM and  
416 HS06 approximation is similar in the tropics,  $P' - E'$  in the extratropics and subtropics is much  
417 more muted in the MEBM. Finally, for Pattern 3 and Pattern 4, when  $\lambda$  is narrowly positive in  
418 the deep tropics and negative across most other latitudes, there is a similar difference between the  
419 MEBM and HS06  $P' - E'$  in the high-latitudes, but the MEBM  $P' - E'$  is larger in the deep tropics.  
420 This increase in the deep tropics far exceeds the HS06 approximation (Eq. 4), and coincides with  
421 a narrowing of the ITCZ where  $P - E > 0$ .

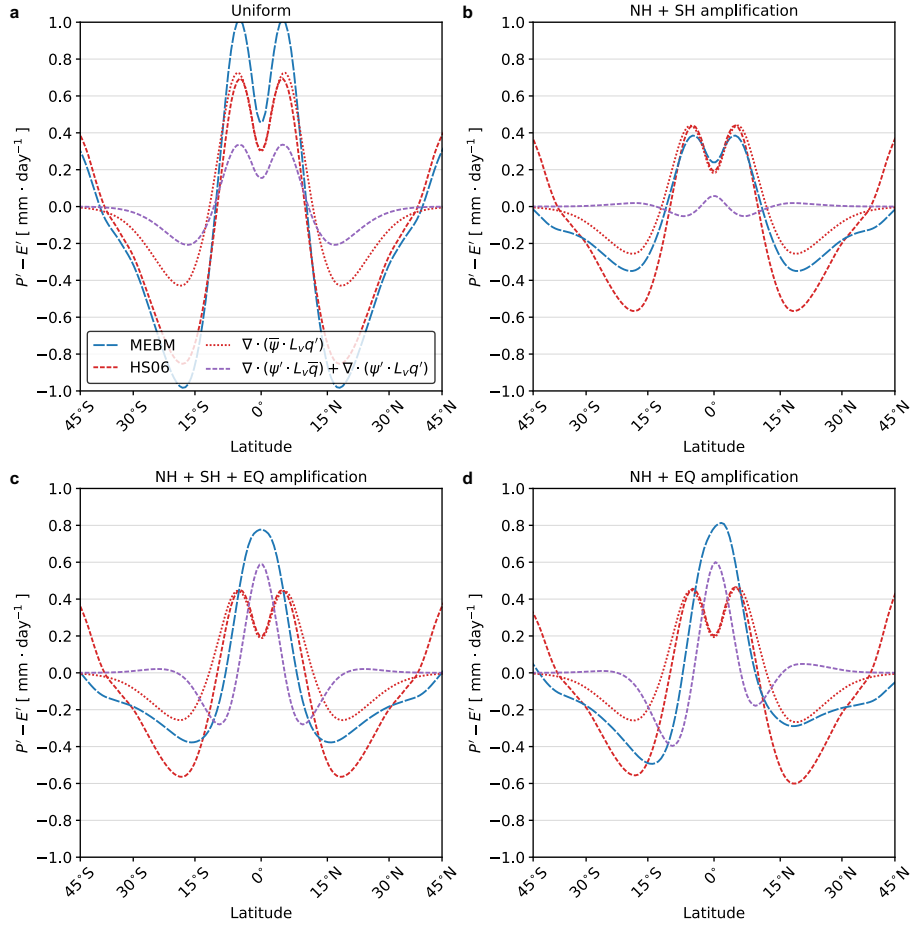
422 To provide a more mechanistic interpretation of how the pattern of  $\lambda$  impacts the pattern of  
423  $P' - E'$ , in the next two subsections we compare the MEBM and HS06 approximation using a set  
424 of simple scalings.

### 425 *b. Tropics*

438 In Figure 1 and Figure 3 we saw that, in the tropics,  $P' - E'$  in the MEBM is much larger than  
439  $P' - E'$  in the HS06 approximation, and is in much better agreement with GCMs. This is also  
440 evident in Figure 7 with the idealized radiative feedback patterns. These differences are likely  
441 related to the MEBM containing a Hadley Cell parameterization that simulates changes to the  
442 Hadley Cell circulation strength under warming. Thus, differences between the MEBM and HS06  
443 approximation in the deep tropics can be understood through the conservation statement for the  
444 atmospheric-moisture budget for  $P - E$  under warming:

$$(P' - E')_{\text{HC}} = -\nabla \cdot \left( \overline{\psi} L_v q' + \psi' L_v \bar{q} + \psi' L_v q' \right), \quad (14)$$

445 where  $\overline{(\cdot)}$  represents the climatological state. Here,  $\overline{\psi}$  and  $\bar{q}$  are derived by applying the MEBM  
446 to the each preindustrial control simulation from 20 GCMs (see Appendix B for details). This  
447 enables us to decompose  $P' - E'$  in the MEBM — for regions where the Hadley Cell accomplishes  
448 most of the latent-energy transport — into thermodynamic and dynamic contributions to  $P' - E'$ .



426 **FIG. 8. Impact of radiative feedback patterns on the tropical hydrological cycle response.** The pattern  
 427 of  $P' - E'$  between  $45^\circ\text{S}$  and  $45^\circ\text{N}$  for a pattern of warming (a) that is uniform, (b) with equal degrees of  
 428 polar amplification in the Northern Hemisphere and Southern Hemisphere, (c) with equal degrees of polar  
 429 amplification in the Northern Hemisphere and Southern Hemisphere and amplified warming on the equator, and  
 430 (d) with more polar amplification in the Northern Hemisphere than Southern Hemisphere and amplified warming  
 431 on the equator. These are calculated following Section 4a (see Fig. 7). The blue dashed line denotes the MEBM  
 432 solution. The red dashed line denotes the Held and Soden (2006) approximation assuming  $\alpha = 7\% \text{ K}^{-1}$  globally.  
 433 The red dotted line is the  $P' - E'$  pattern with no circulation strength changes and changes to the moisture content  
 434 of the atmosphere,  $\nabla \cdot (\bar{\psi} L_v q')$ . The purple dashed line is the  $P' - E'$  pattern with circulation strength changes  
 435 and changes to the moisture content of the atmosphere,  $\nabla \cdot (\psi' L_v \bar{q}) + \nabla \cdot (\psi' L_v q')$ . Note that the latitude range  
 436 is confined to  $45^\circ$  as this is where the Hadley Cell parameterization exhibits little-to-no influence on moisture  
 437 transport.

449 Broadly, the first term represents no changes to the strength of the Hadley Cell and changes to  
 450 the moisture content of the atmosphere (which is nearly equivalent to Eq. 4); the second term  
 451 represents changes to the strength of the Hadley Cell and no changes to the moisture content of the  
 452 atmosphere; and the third term is second-order and combines changes to the strength of the Hadley  
 453 Cell and moisture changes.

454 Figure 8 shows  $P' - E'$  for each pattern of  $\lambda$  into contributions from the three terms in Eq. (14),  
 455 in the region influenced by the Hadley Cells (45°S to 45°N). Under a uniform pattern of warming  
 456 (Fig. 8a) the thermodynamic term (red dotted line) dominates  $P' - E'$  while the two dynamical  
 457 terms (purple line) simply amplify the existing pattern of  $P - E$ , with no change in the spatial  
 458 structure of  $P - E$ . Note that the thermodynamic term, which does not represent changes to the  
 459 strength of the Hadley Cell, is nearly equivalent to the HS06 approximation in the deep tropics.  
 460 Similarly, under a pattern of warming with equal degrees of polar amplification in each hemisphere  
 461 and uniform warming throughout the tropics (Fig. 8b), the thermodynamic term (red dotted line)  
 462 again dominates  $P' - E'$  and there is little-to-no change in the spatial pattern of  $P - E$  in the deep  
 463 tropics from the dynamical terms (purple line). However, under a pattern of warming with equal  
 464 degrees of polar amplification in each hemisphere (Fig. 8c), but more warming near the equator,  
 465 the dynamical terms dominate  $P - E$  changes in the deep tropics. Here,  $\psi'$  causes an enhancement  
 466 of  $P - E$  in the deep tropics. Between 5°S and 5°N, changes to  $\psi$  contribute to an enhancement  
 467 of approximately 5 mm day<sup>-1</sup> in  $P - E$ . Likewise, under amplified warming of the Arctic, more  
 468 muted Southern Hemisphere warming, and amplified warming near the equator (Fig. 8d), there is  
 469 larger  $P - E$  in the deep tropics, which also arises mainly from changes in  $\psi$ .

470 Because the Hadley Cells greatly impact  $P' - E'$  in the deep tropics, we now focus on the  
 471 mechanisms responsible for the mass-flux changes in the MEBM. To do this, we turn to Eq. (10),  
 472 which relates the strength of the Hadley Cell to the poleward heat flux and gross moist stability.  
 473 Rearranging for  $\psi'(x)$  gives:

$$\psi'(x) = \underbrace{\frac{F'_{\text{HC}}}{\bar{H} + H'}}_{\psi'_1} - \underbrace{\frac{\bar{\psi}H'}{\bar{H} + H'}}_{\psi'_2}, \quad (15)$$

474 where  $\psi'_1$  represents changes to  $\psi$  that result from changes in the poleward heat transport by the  
 475 Hadley Cell and  $\psi'_2$  represents changes to  $\psi$  that result from changes in gross moist stability, or the  
 476 stratification of the tropical atmosphere. Note that gross moist stability always scales at 8% above

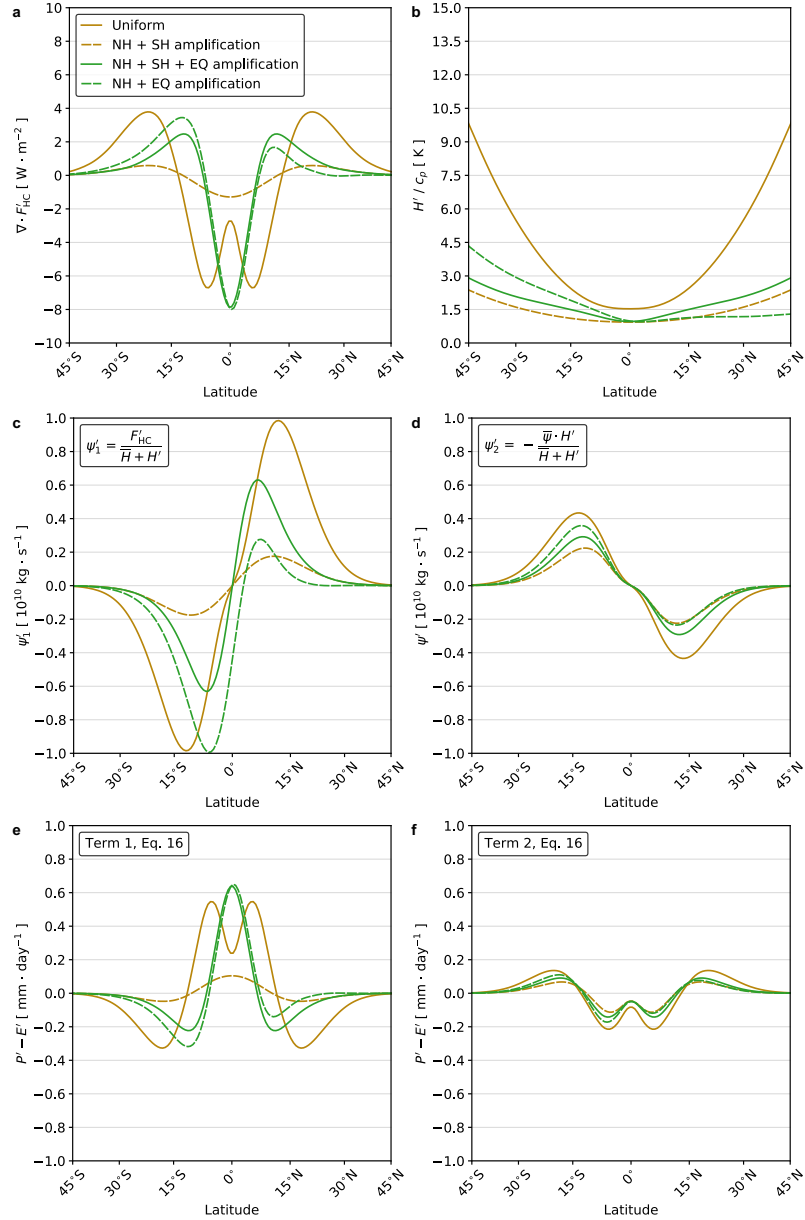
477 the equator value of  $h'_0$ , but can change due to changes in  $h'$ . These two terms can be combined  
 478 with Eq. (14) to produce:

$$(P' - E')_{\text{HC}} = -\nabla \cdot \left( \bar{\psi} L_v q' + \underbrace{(\psi'_1 L_v \bar{q} + \psi'_1 L_v q')}_{\text{Term 1}} + \underbrace{(\psi'_2 L_v \bar{q} + \psi'_2 L_v q')}_{\text{Term 2}} \right), \quad (16)$$

479 where now  $P' - E'$  can be decomposed into three terms: a thermodynamic term with no circulation  
 480 strength changes but changes to the moisture content of the atmosphere (i.e., Eq. 4), and two  
 481 dynamic terms that represent circulation strength changes from either the poleward heat transport  
 482 by the Hadley Cell (Term 1) or changes in gross moist stability (Term 2).

491 Figure 9 shows the divergence of anomalous atmospheric heat transport (Fig. 9a) and anomalous  
 492 gross moist stability (Fig. 9b) for each of the four  $\lambda$  patterns. These two variables can be used to  
 493 decompose changes to the Hadley Cell circulation strength into the two terms from Eq. (15) (see  
 494 Fig. 9c-d). The decomposition shows that changes to the poleward heat transport by the Hadley  
 495 Cell (i.e., Term 1) largely act to strengthen  $\psi$ , and that changes to gross moist stability (i.e., Term  
 496 2) largely act to weaken  $\psi$  (Fig. 9). With a pattern of  $\lambda$  that produces uniform warming there is  
 497 excess energy in the tropics that must be exported poleward (see solid gold line in Fig. 9a), driving  
 498 a stronger  $\psi$  (see solid gold line in Fig. 9c). Uniform warming also acts to produce the largest  
 499 gross moist stability changes (see solid gold line in Fig. 9b), which weakens  $\psi$  (see solid gold line  
 500 in Fig. 9d). The changes in gross moist stability are consistent with Chou et al. (2013), who found  
 501 that increases in gross moist stability are related to a weakening of  $\psi$ . However, these changes are  
 502 much smaller than the poleward heat changes and there is no change in the spatial structure of  $\psi'$   
 503 and therefore  $P' - E'$  increases largely following the climatological state (see solid gold line in Fig.  
 504 9e-f). This is also true for a uniform pattern of  $\lambda$ , where there are smaller changes to  $\psi$ , but again  
 505 little-to-no change to the spatial structure of  $\psi$  (see dashed gold line in Fig. 9c-d).

506 With a pattern of  $\lambda$  that is less negative in the tropics and much more narrowly peaked — which  
 507 is similar to the patterns of  $\lambda$  in GCMs — a different story emerges. Here, the small bump in  
 508 warming in the deep tropics leads to an excess of energy in the deep tropics (see green lines in  
 509 Fig. 9a). This drives a stronger Hadley Cell in the deep tropics because of an increasing poleward  
 510 heat flux (see green lines in Fig. 9c). The excess energy of the deep tropics cannot be radiated



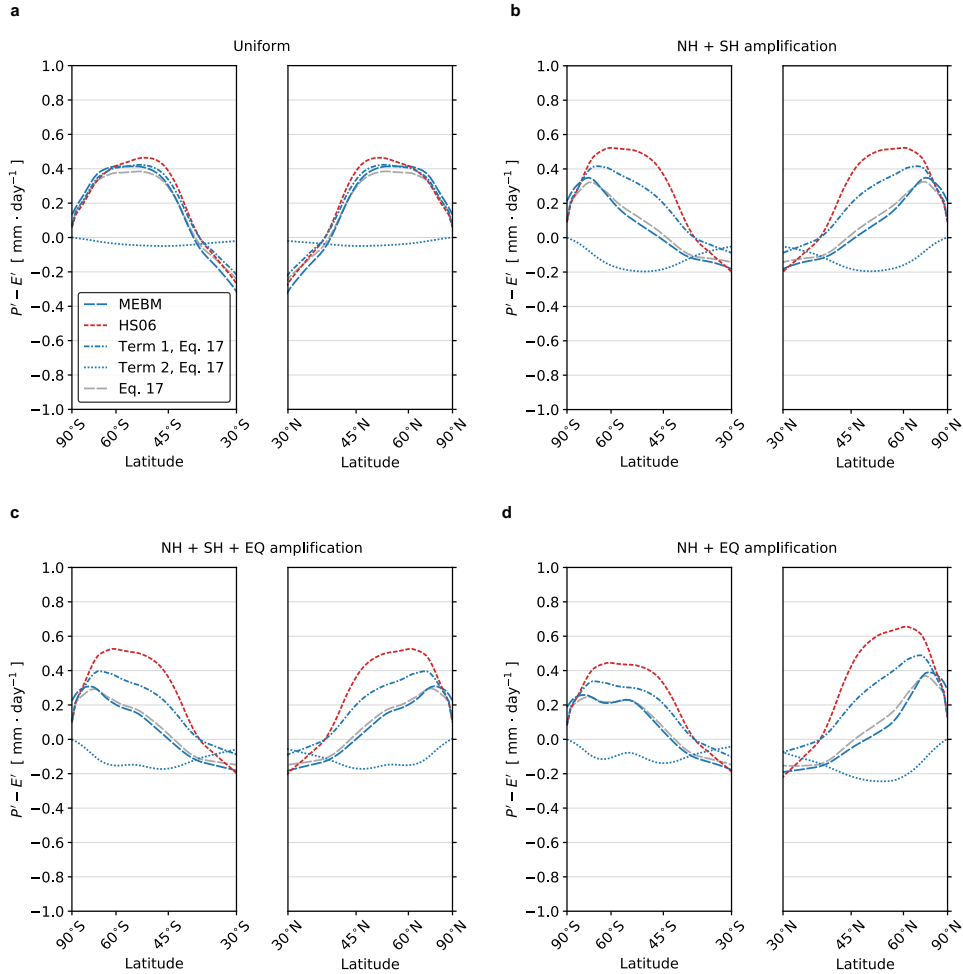
483 **FIG. 9. Mechanisms for the influence of radiative feedbacks on the response of the tropical hydrological**  
 484 **cycle.** Changes to (a) the divergence of atmospheric energy transport by the Hadley Cells ( $\nabla \cdot F'_{HC}$ ) and (b)  
 485 gross moist stability ( $H'$ ). Changes to the southward mass transport by the parameterized Hadley Cells, which  
 486 is the sum of changes due (c) to the net atmospheric energy transport and (d) to gross moist stability changes.  
 487  $P - E$  changes (e) from Term 1 and (f) Term 2 from (c) and (d), respectively (see Eq. 16). The gold solid line  
 488 denotes the uniform warming case. The gold dashed line denotes the polar-amplified warming case. The purple  
 489 solid line denotes the polar-amplified warming and Equator warming case. The purple dashed line denotes the  
 490 Arctic-amplified warming and Equator warming case.

511 away locally and must be exported to higher-latitudes, or regions of more efficient radiative loss.  
 512 However, the structure of  $\lambda$  determines where this energy can go and hence the response of  $\psi$ :  
 513 strengthening  $\psi$  in the deep tropics more than  $\psi$  in the subtropics (see green lines Fig. 9c). In other  
 514 words, the fact that  $\lambda$  peaks near the equator and tapers off toward the subtropics means that  $\psi$   
 515 strengthens slightly more in the deep tropics relative to the subtropics, helping to change its spatial  
 516 structure (Fig. 9c). Furthermore, because  $R_f$  and  $G'$  are spatially uniform, any spatial structure in  
 517  $\lambda$  must be balanced by the spatial structure of  $\nabla \cdot F'_{\text{HC}}$  or  $T'$ . And because  $\nabla \cdot F'_{\text{HC}}$  contains more  
 518 spatial structure than  $T'$ , the pattern of  $\lambda$  ultimately drives the  $P - E$  changes through the pattern  
 519 of  $\nabla \cdot F'_{\text{HC}}$ . The change to the spatial structure of  $\psi$  acts to increase  $P - E$  in the deep tropics and  
 520 decrease  $P - E$  in the subtropics, which narrows the ITCZ region (Fig. 9e).

521 Term 2, which represents changes to  $\psi$  from gross moist stability changes, is small and cannot  
 522 oppose the changes to  $\psi$  in the deep tropics that results from changes to the poleward heat transport  
 523 by the Hadley Cell (Fig. 9d). However, in the subtropics the weakening of  $\psi$  outcompetes the  
 524 strengthening of  $\psi$  from an increase poleward heat flux (compare Fig. 9c and Fig. 9d). The  
 525 weakening of  $\psi$  from Term 2 acts to decrease  $P - E$  at the edges of the ITCZ region (Fig. 9f). In  
 526 other words, the pattern of radiative feedbacks causes anomalous energy to be exported from the  
 527 tropics to the poles, strengthening  $\psi$ . At the same time, the increase in gross moist stability weakens  
 528  $\psi$ , but this weakening is confined mainly to the subtropics. This occurs because of larger increases  
 529 to the moist-static energy gradient in the subtropics when compared to the tropics. Together, in  
 530 unison, these two processes determine the degree of ITCZ contraction. These circulation changes  
 531 are similar to Feldl and Bordoni (2016), where the Hadley Cell was found to strengthen in the  
 532 deep tropics and weaken in the subtropics under warming. In Section 4d we directly compare the  
 533 mass-flux changes in the MEBM and GCMs.

### 534 *c. Extratropics*

547 In the extratropics,  $P' - E'$  from the MEBM and the HS06 approximation are approximately equal  
 548 under uniform warming (Fig. 7a), but are different under polar-amplified warming (Fig. 7b-d).  
 549 Under polar-amplified warming the MEBM predicts less enhancement of high-latitude  $P - E$  than  
 550 HS06, and is in better agreement with the GCMs (see Fig. 1a and Figs. 3). The MEBM also  
 551 predicts an expansion of the subtropical regions (see Section 1 and 3). To understand how these



535 **FIG. 10. Impact of radiative feedback patterns on the extratropical hydrological cycle response.** The  
 536 pattern of  $P' - E'$  poleward of  $30^\circ\text{S}$  and  $30^\circ\text{N}$  for a pattern of warming: (a) that is uniform; (b) with equal degrees  
 537 of polar amplification in the Northern Hemisphere and Southern Hemisphere; (c) with equal degrees of polar  
 538 amplification in the Northern Hemisphere and Southern Hemisphere and amplified warming on the equator; and  
 539 (d) with more polar amplification in the Northern Hemisphere than Southern Hemisphere and amplified warming  
 540 on the equator (see Fig. 7). These are found following Section 4a (see Fig. 7). The blue dashed line denotes the  
 541 MEBM solution. The red dashed line denotes the Held and Soden (2006) approximation assuming  $\alpha = 7\% \text{ K}^{-1}$   
 542 globally. The blue dash-dotted line is the  $P' - E'$  pattern from term one in Eq. (17), which represents changes  
 543 to moisture content of the atmosphere with no changes to the transport of moisture. The blue dotted line is the  
 544  $P' - E'$  pattern from term two in Eq. (17), which represents changes to the transport of moisture under warming.  
 545 The grey dashed line is the  $P' - E'$  pattern with transport changes included in addition to the full spatial structure  
 546 of  $\beta$  (Eq. 17).

552 differences arise, we use an extended version of the simple scaling from HS06, which is detailed  
 553 in Siler et al. (2018). Appendix C contains relevant details of the derivation, but this scaling  
 554 decomposes  $P' - E'$  in the extratropics into two terms via:

$$P' - E' = \underbrace{\beta(P - E)}_{\text{Term 1}} - \underbrace{\frac{1}{2\pi a^2} F_L \frac{d\beta}{dx}}_{\text{Term 2}}, \quad (17)$$

555 where:

$$\beta = \left( \alpha - \frac{2}{T} \right) T' + \frac{dT'/dx}{dT/dx}. \quad (18)$$

556 Eq. (17) implies that the pattern of  $P' - E'$  is amplified under global warming by a factor of  $\beta(x)$ .  
 557 Term 1 represents changes to the moisture content of the atmosphere, while Term 2 represents  
 558 changes to the poleward moisture transport by eddies. HS06 argue that Eq. (17) can be simplified  
 559 to Eq. (4) by ignoring changes in the pattern of warming, which means that  $\beta$  is approximately  
 560 uniform and thus Term 2 in Eq. (17) is close to zero, making  $P' - E' \approx \beta(P - E) = \alpha T' (P - E)$ ,  
 561 or exactly Eq. (4). These arguments make sense for uniform warming, which indeed leads to  
 562 Term 2 in Eq. (17) being close to zero and the structure of  $P' - E'$  is simply the existing pattern  
 563 of  $P - E$  amplified by the pattern of warming, which is consistent with Fig. 7c. However, under  
 564 polar-amplified warming these arguments make less sense, as strong meridional variations in  $T'$   
 565 act to alter both Term 1 and Term 2.

566 Figure 10 shows a decomposition of  $P' - E'$  for each pattern of  $\lambda$  in the Northern and Southern  
 567 Hemisphere extratropics (poleward of  $30^\circ$ ) using the two terms in Eq. (17), the MEBM solution,  
 568 and the HS06 approximation from Figure 7. Under uniform warming, where the MEBM and HS06  
 569 approximation are approximately equal, the contribution of changes to the poleward moisture  
 570 transport is relatively small (Fig. 10a). This occurs because  $dT'/dx = 0$ , making  $\beta$  relatively  
 571 uniform and thus the transport of moisture (i.e., Term 2 in Eq. 17) is close to zero and contributes  
 572 little to  $P' - E'$ . However, under polar-amplified warming the MEBM and HS06 approximation  
 573 diverge because of changes to spatial structure of  $\beta$  and changes to the poleward moisture transport  
 574 (Fig. 10b-d). Because  $T'$  increases with latitude, the meridional temperature gradient weakens and  
 575 therefore  $\beta$  decreases everywhere, which partially offsets the Clausius-Clapeyron effect. A similar  
 576 feature is seen in under an asymmetric pattern of warming (Fig. 10d). When warming is amplified

577 mainly in the Arctic, there is a reduction of  $P' - E'$  equal to approximately  $2 \text{ mm year}^{-1}$  uniformly  
578 in the Northern Hemisphere extratropics. This decrease in poleward moisture transport reduces  
579 the enhancement of  $P' - E'$  in the high latitudes, and brings the MEBM in line with results from  
580 GCMs.

#### 581 *d. Connection to CMIP5 hydrological changes*

582 Armed with a better understanding of processes that set the pattern of  $P' - E'$  in the tropics and  
583 extratropics, we now revisit the ability of the MEBM to emulate comprehensive GCMs in CMIP5  
584 using the same scalings from the previous sections.

#### 585 1) TROPICAL HYDROLOGICAL CHANGES

586 Figure 11 shows a decomposition of  $P' - E'$  associated with the three terms of Eq. (14),  
587 which detail thermodynamic and dynamic changes to  $P - E$  under warming. This is the same  
588 decomposition shown in Figure 8, but for each individual GCM. Across most GCMs, changes to  $\psi$   
589 are large and have a large impact on the  $P - E$  changes in the deep tropics. The change in  $\psi$  results  
590 in enhancement of  $P - E$  in the deep tropics. Between  $5^\circ\text{S}$  and  $5^\circ\text{N}$ , changes to  $\psi$  contribute to  
591 an enhancement of approximately  $6 \text{ mm day}^{-1}$  in  $P - E$ . In GCMs with larger  $P - E$  changes in  
592 the deep tropics (e.g., ACCESS1.0 and MIROC-ESM),  $\nabla \cdot (\psi' L_v \bar{q})$  and  $\nabla \cdot (\psi' L_v q')$  contributes  
593 to  $8 - 9 \text{ mm day}^{-1}$  in  $P - E$  changes. Conversely, in GCMs with smaller  $P - E$  changes in the  
594 deep tropics (e.g., CCSM4 and INM-CM4),  $\nabla \cdot (\psi' L_v \bar{q})$  and  $\nabla \cdot (\psi' L_v q')$  contributes  $3 - 4 \text{ mm}$   
595  $\text{day}^{-1}$  in  $P - E$  changes. Additionally, GCMs with stronger hemispheric asymmetry in subtropical  
596 drying (e.g., GFDL-ESM2M, HadGEM2-ES) exhibit this asymmetry because of the dynamical  
597 terms (purple line).

598 Indeed,  $P - E$  changes in the deep tropics are significantly impacted by changes in circulation  
599 strength. The mechanism for this is detailed in Figure 9 and related to the fact that some GCMs  
600 exhibit a narrowly peaked pattern of less negative or even positive values in the deep tropics near  
601 the equator. This radiative feedback pattern implies more strengthening of  $\psi$  around the equator  
602 and less strengthening (or weakening) of  $\psi$  in the subtropics, thereby changing the spatial structure  
603 of  $\psi$ . In fact, the average feedback value in the deep tropics (averaged between  $5^\circ\text{S}$  and  $5^\circ\text{N}$ ) is  
604 strongly correlated ( $r = 0.68$ ) with the  $P' - E'$  values between  $5^\circ\text{S}$  and  $5^\circ\text{N}$ . Similarly, the average  
605

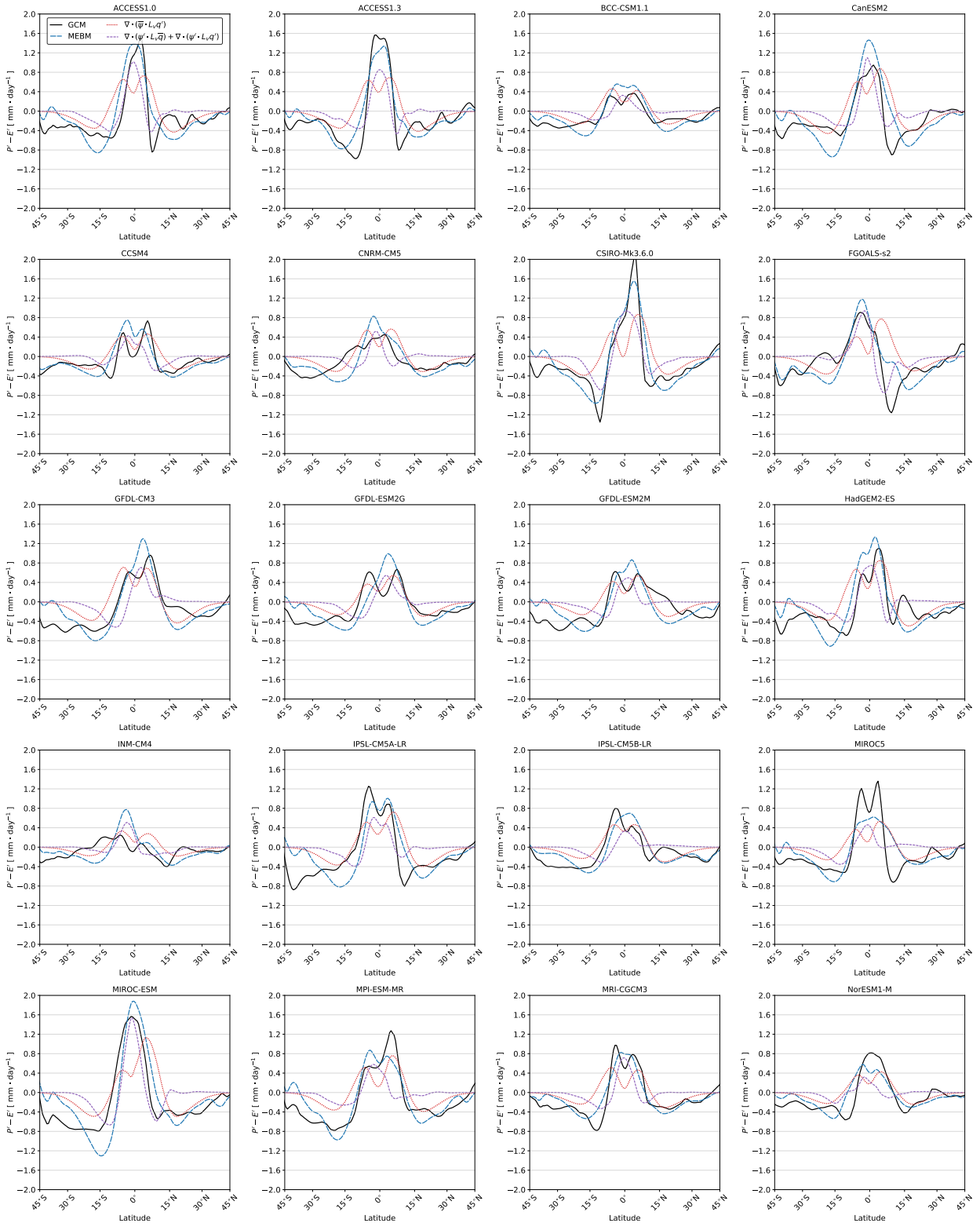


FIG. 11. See next page.

586 **FIG. 11. Tropical hydrological changes in CMIP5.** The pattern of  $P' - E'$  between  $45^\circ\text{S}$  and  $45^\circ\text{N}$  for each  
587 GCM. The black line denotes the GCM. The blue dashed line denotes the MEBM solution. The red dotted line  
588 is the  $P' - E'$  pattern from the MEBM with no circulation strength changes and changes to the moisture content  
589 of the atmosphere,  $\nabla \cdot (\bar{\psi} L_v q')$ . The purple dashed line is the  $P' - E'$  pattern from the MEBM with circulation  
590 strength changes and changes to the moisture content of the atmosphere,  $\nabla \cdot (\psi' L_v \bar{q}) + \nabla \cdot (\psi' L_v q')$ . Note that the  
591 latitude range is confined to  $45^\circ$  as this is where the Hadley Cell parameterization begins to exhibit little-to-no  
592 influence on moisture transport.

612 divergence of the northward column-integrated atmosphere energy transport averaged between  $5^\circ\text{S}$   
613 and  $5^\circ\text{N}$  is also strongly correlated ( $r = 0.72$ ) with the  $P' - E'$  values between  $5^\circ\text{S}$  and  $5^\circ\text{N}$ . This  
614 highlights the importance of radiative feedbacks in setting poleward heat transport, which acts to  
615 strengthen the Hadley Cell circulation in the deep tropics and enhance  $P - E$ .

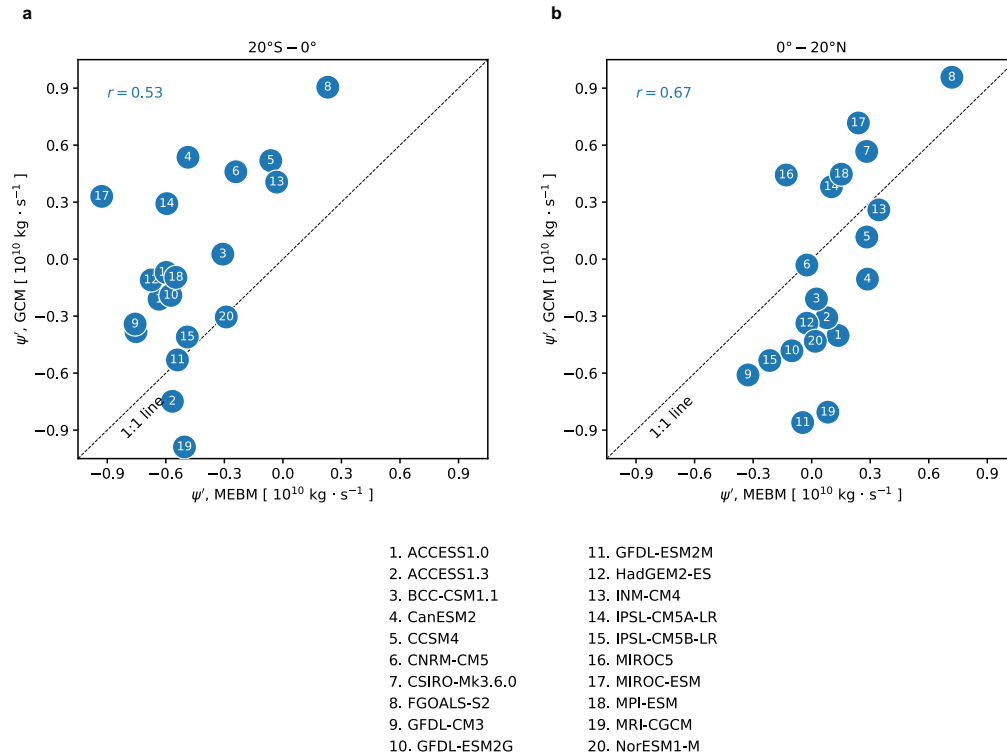
616 The skill of the MEBM in emulating the Hadley Cell mass-flux changes is further compared with  
617 the actual streamfunction of the CMIP5 GCMs, which is calculated as:

$$\psi(x, p) = \frac{2\pi a}{g} \sqrt{(1-x^2)} \int_0^{p_s} [\bar{v}] dp, \quad (19)$$

618 where  $[\bar{v}]$  is zonal-mean and time-mean meridional velocity as a function of latitude and pressure  
619  $p$ . To compare the Hadley Cell mass flux of each GCM with the MEBM, we take the maximum  
620 magnitude (positive or negative) of the meridional mass streamfunction in Eq. (19) to produce the  
621 CMIP5 Hadley Cell mass-flux strength  $\psi_{\max}(x)$ .

622 The strengthening of the Hadley Cell in the deep tropics and the weakening of the subtropics in the  
623 MEBM is consistent with the response from CMIP5 GCMs, but the MEBM tends to underpredict  
624 changes to  $\psi_{\max}$  in each hemisphere, which can be seen in Figure 12. However, the average mass-  
625 flux change of the MEBM in the deep tropics of the Southern Hemisphere ( $20^\circ\text{S} - 0^\circ$ ) and Northern  
626 Hemisphere ( $0^\circ - 20^\circ\text{N}$ ) is well correlated ( $r = 0.53$  and  $r = 0.67$ ) with the Hadley Cell mass-flux  
627 change in CMIP5 (Fig. 12). Further work is required to understand the precise reasons why the  
628 MEBM and the CMIP5 GCMs agree well and how these results connect to the dynamical theories  
629 of the Hadley Cell circulation. Furthermore, it is unclear here if the pattern of radiative feedbacks  
630 arise from the circulation changes and the MEBM simply captures this relationship. Nonetheless,

631 the agreement suggests that down-gradient energy transport provides a strong constraint on the  
 632 Hadley Cell mass-flux changes and tropical  $P - E$  changes.



633 FIG. 12. **Comparison of the Hadley Cell mass-flux changes.** Scatter plots of the area-averaged Hadley Cell  
 634 mass-flux change in each GCM and MEBM simulation from (a) 20°S to 0° and (b) 0° to 20°N. The top left  
 635 corner of the plot shows the Pearson correlation coefficient between MEBM and GCM.

## 636 2) EXTRATROPICAL HYDROLOGICAL CHANGES

642 Figure 13 shows a decomposition of  $P' - E'$  poleward of 30° into the two terms from Eq. (17),  
 643 which represent changes to the moisture content of the atmosphere and changes to the poleward  
 644 moisture flux. This is the same decomposition shown in Figure 10, but for each individual GCM.  
 645 Across all GCMs it is evident that reduced poleward moisture transport helps to align the MEBM  
 646 with GCMs. The poleward moisture transport (i.e., Term 2) decreases in both hemispheres across  
 647 most GCMs and accounts for 1 – 2 mm day<sup>-1</sup> decrease in  $P - E$ . The reduced poleward moisture  
 648 transport also causes the expansion of the subtropics in each GCM, which is shown by the more  
 649 poleward latitude of  $P - E = 0$ . While not shown in Figure 12, GCMs with a stronger polar

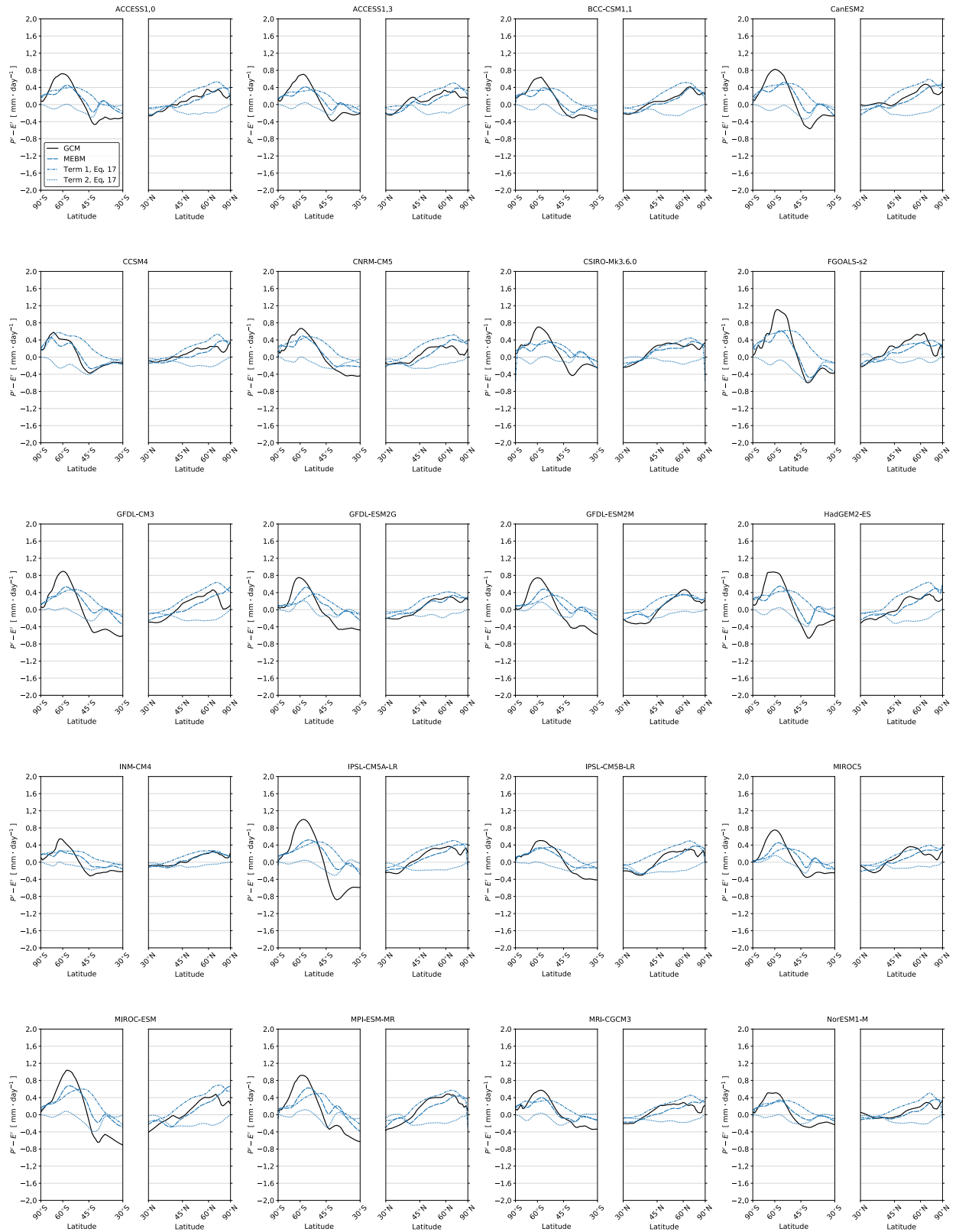


FIG. 13. See next page.

637 FIG. 13. **Extratropical hydrological changes in CMIP5.** The pattern of  $P' - E'$  poleward of  $30^\circ$ . The black  
638 line denotes the GCM response. The blue dashed line denotes the MEBM solution. The blue dash-dotted line is  
639 the  $P' - E'$  pattern from term one in Eq. (17) using MEBM output, which represents changes to moisture content  
640 of the atmosphere with no changes to the transport of moisture. The blue dotted line is the  $P' - E'$  pattern from  
641 term two in Eq. (17) using MEBM output, which represents changes to the transport of moisture under warming.  
650 amplification tend to have a stronger reduction in the poleward moisture transport, and stronger  
651 subtropical drying.

## 652 5. Discussion and conclusions

653 Changes to  $P - E$  over the 21st century are predicted to impact ecosystems and socioeconomic  
654 activities throughout the world. While it is expected that, broadly, dry regions will get drier and  
655 wet regions will get wetter, the magnitude and spatial structure of  $P - E$  changes remains uncertain.

656 In this paper, we examined the response of  $P - E$  to warming using a modified MEBM that  
657 reroutes moisture transport in the deep tropics with a Hadley-Cell parameterization (Siler et al.  
658 2018). We showed that the MEBM accurately emulates  $P - E$  changes and accounts for a majority  
659 of the intermodel variance in  $P - E$  changes as simulated by GCMs under greenhouse-gas forcing.  
660 We then used the MEBM to identify sources of uncertainty in the pattern of  $P' - E'$  under warming.  
661 Using zonal-mean patterns of radiative forcing  $R_f$ , ocean heat uptake  $G'$ , and the net radiative  
662 feedback  $\lambda$  from a suite of GCMs under  $4 \times \text{CO}_2$ , we showed that the MEBM accounts for the  
663 majority of the intermodel variance in  $P - E$  in the deep tropics, subtropics, and extratropical  
664 high-latitudes. The intermodel spread in  $P' - E'$  in these regions arises primarily from intermodel  
665 differences in  $\lambda$ , with  $R_f$  and  $G'$  playing secondary roles. However, in regions where regional  
666 ocean circulation shapes the rate of warming,  $G'$  can account for 30–40% of the intermodel  
667 variance in  $P - E$  changes. Finally, by confining the intermodel spread of  $\lambda$  to different regions, we  
668 showed that intermodel variations in tropical  $\lambda$  impact  $P - E$  changes globally, whereas intermodel  
669 variations in polar  $\lambda$  mainly impact  $P - E$  changes in the poles.

670 Motivated by the fact that  $\lambda$  plays a leading role in setting the pattern of  $P - E$ , we constructed  
671 a set of idealized  $\lambda$  patterns and used some extended scalings to further investigate the processes  
672 impacting  $P' - E'$ . We demonstrated that  $P - E$  changes depend crucially on the meridional pattern  
673 of warming and the anomalous net energy input into the atmosphere. Under uniform warming,

674  $P - E$  changes at approximately the Clausius-Clapeyron rate, consistent with the thermodynamic  
675 scaling first introduced by HS06. However, under polar-amplified warming, moisture transport  
676 to the high-latitudes decreases, causing less of an increase in  $P - E$  in the high-latitudes when  
677 compared to the HS06 approximation. Interestingly, when  $\lambda$  is less negative near the equator and  
678 begins to taper off in the subtropics,  $P - E$  in the deep tropics increases and the ITCZ region narrows,  
679 deviating strongly from the thermodynamic scaling of HS06. This occurs because the anomalous  
680 net energy input into the atmosphere cannot be radiated away locally at the equator, which means  
681 the Hadley Cell mass flux  $\psi$  must strengthen in the deep tropics to transport that excess energy  
682 away. However, the concurrent increase in gross moist stability, which weakens  $\psi$ , outcompetes the  
683 poleward heat transport changes in the subtropics, where moist-static energy gradients are stronger.  
684 These two processes change the spatial structure of  $\psi$  and cause a convergence of moisture in the  
685 deep tropics, increasing  $P - E$  in the tropics and decreasing  $P - E$  in the subtropics. Of course,  
686 it is possible that the  $\lambda$  patterns themselves result from these circulation changes, and our results  
687 simply confirm the tightly coupled nature of hydrological changes and radiative response in the  
688 deep tropics. Still, our results demonstrate the importance for circulation changes and how radiative  
689 feedbacks relate to them. More work is required to understand whether the circulation responses  
690 give rise to the radiative feedbacks and the radiative feedbacks simply reflect these changes. Finally,  
691 under asymmetric warming, where warming is more amplified in the Arctic when compared to  
692 the Antarctic, we find the subtropics dry less in the Northern Hemisphere when compared to  
693 the Southern Hemisphere. This mimics the hemispheric asymmetry of subtropical drying seen  
694 in GCMs and is traced to the asymmetric response of the changing atmospheric circulation.  
695 These circulation-strength changes can be understood as a consequence of the demands of overall  
696 downgradient energy transport, as encapsulated in the MEBM.

697 Our study has several implications. Given the role of polar amplification in setting the magnitude  
698 of the poleward moisture flux, the large spread in Arctic amplification among GCMs (Pithan and  
699 Mauritsen 2014; Bonan et al. 2018; Feldl et al. 2020) may also explain the large uncertainty in  $P - E$   
700 changes, particularly for the Northern Hemisphere extratropics. Similarly, the relative warming  
701 of the Arctic versus the Antarctic, and the processes contributing to this asymmetry may explain  
702 intermodel differences in the amount of subtropical drying between each hemisphere by affecting  
703 the poleward heat flux, and thus the strength of the Hadley Cell circulation. Furthermore, the role

704 that radiative feedbacks play in setting  $P - E$  changes under warming suggests that studying the  
705 effect of each individual radiative feedback may help identify limits of the “wet-gets-wetter, dry-  
706 gets-drier” paradigm, and offer insights into potential biases in GCMs. Finally, our results indicate  
707 that changes to large-scale tropical circulations can be energetically-constrained with a simple rule  
708 of downgradient energy transport, and that this rule helps to explain the narrowing of the ITCZ  
709 and hemispheric asymmetry in subtropical drying. Understanding how energetic constraints can  
710 be used to understand other dynamical features in GCMs (e.g., Feldl and Bordoni 2016) or the  
711 seasonality of  $P - E$  changes should be the subject of future work.

712 This study, however, contains a few caveats. In the MEBM the spatial patterns of  $R_f$ ,  $\lambda$ ,  
713 and  $G'$  are prescribed and do not change over time. Thus, we are unable to consider transient  
714  $P - E$  changes under global warming or the extent to which the spatial patterns of  $\lambda$  and  $G'$   
715 are truly independent of atmospheric energy transport and the circulation responses themselves.  
716 Furthermore, the assumption that  $D$  is spatially uniform and invariant under warming is surely a  
717 crude approximation. Previous work has shown that  $D$  can be approximately 75% larger in the  
718 mid-latitudes when compared to the subtropics (Frierson et al. 2007; Peterson and Boos 2020)  
719 and can affect the degree of meridional shifts in tropical rainfall (Peterson and Boos 2020).  $D$   
720 has also been shown to decrease under sustained greenhouse-gas forcing (Shaw and Voigt 2016;  
721 Mooring and Shaw 2020). Future work might explore the impact of spatial patterns of  $D$ . Finally,  
722 the Hadley Cell parameterization is limited as it does not account for (1) changes between latent-  
723 energy transport accomplished by eddies and the Hadley Cell under warming; or (2) changes to the  
724 structure of upper-tropospheric moist-static energy under warming. For instance, the disagreement  
725 between subtropical  $P' - E'$  in MEBM and GCMs is likely related to the fact that the Hadley Cell  
726 mass-flux change is small outside of the deep tropics and systematically underestimated in the  
727 MEBM. Future work might also explore the impact of allowing for the Hadley Cell edge to change  
728 under warming (e.g., O’Gorman and Schneider 2008; Mbengue and Schneider 2018) or better  
729 parameterizations of gross moist stability like making it proportional to the meridional gradient in  
730 moist static energy (e.g., Frierson 2008) and unique to each GCM.

731 Despite these shortcomings, the fact that the MEBM emulates  $P - E$  changes as simulated in  
732 GCMs under greenhouse-gas forcing, suggests that the MEBM and the processes it represents offers  
733 a parsimonious understanding of the causes of hydrological change that is distinct from the simple

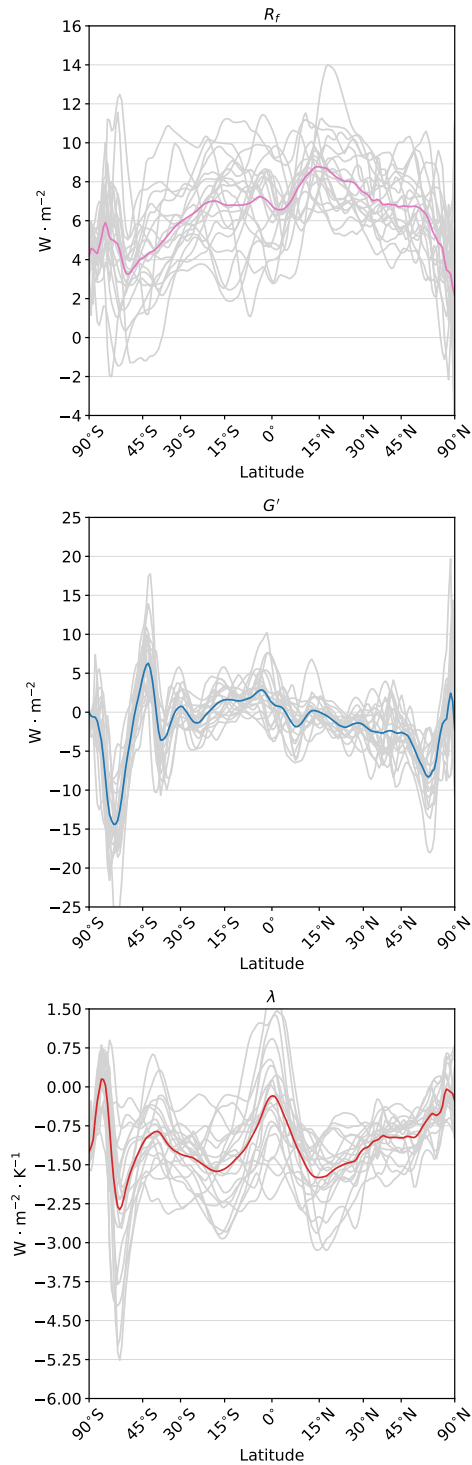
734 thermodynamic scaling that results in the “wet-gets-wet, dry-gets-drier” paradigm. Specifically, in  
735 this paper, we showed how the MEBM captures changes to moisture transport in both the tropics  
736 and high-latitudes that is not captured in other hydrological scalings. This work demonstrates that  
737 the spatial structure of radiative feedbacks can greatly impact changes to the strength of the Hadley  
738 Cell circulation, acting to increase  $P - E$  in the deep tropics, decrease  $P - E$  in the subtropics,  
739 and narrow the ITCZ. This work also demonstrates the utility of downgradient energy transport to  
740 examine drivers of the intermodel spread in  $P - E$  changes. Our results suggest that, for as long as  
741 tropical feedbacks and polar amplification remain uncertain and poorly constrained among GCMs,  
742 projections of the spatial pattern of hydrological change will also remain uncertain. More broadly,  
743 our results imply that downgradient energy transport and energetic constraints on the strength of  
744 the Hadley Cell circulation provide an alternative and perhaps more fundamental explanation for  
745 the response of  $P - E$  to climate change.

## 746 APPENDIX A

### 747 CMIP5 output

748 We use monthly output from 20 different GCMs participating in Phase 5 of the Coupled Model  
749 Intercomparison Project (CMIP5; Taylor et al. 2012). This subset of GCMs reflects those that  
750 provide the necessary output for calculating  $R_f(x)$ ,  $G'(x)$ , and  $\lambda(x)$ . For each GCM, we calculate  
751 anomalies in each variable, denoted by prime, as the difference between the variable averaged  
752 over a preindustrial control simulation and the variable averaged over the last 25 years of  $4 \times \text{CO}_2$   
753 simulations (years 126 – 150). All variables are annual- and zonal- means computed from monthly  
754 output. The variables include: all-sky shortwave and longwave radiation at the surface and top of  
755 atmosphere (rsds, rsus, rsdt, rsut, rlds, rlus, rlut), sensible and latent heat fluxes (hfss, hfls), sea  
756 surface temperature (tos), near-surface air temperature (tas), precipitation (pr), and evaporation  
757 (evs).

758  $R_f(x)$  is calculated from the change in top of atmosphere (TOA) radiation in  $4 \times \text{CO}_2$  simulations  
759 performed with fixed preindustrial sea-surface temperatures (Siler et al. 2019).  $G'(x)$  is calculated  
760 as the change in net surface heat fluxes in  $4 \times \text{CO}_2$  simulations performed in fully coupled GCMs.  
761  $\lambda(x)$  is calculated by equating the zonal-mean net TOA radiation anomaly with  $\lambda(x)T'(x) + R_f(x)$ .  
762 Figure A1 shows the patterns of  $R_f(x)$ ,  $G'(x)$ , and  $\lambda(x)$  for each GCM.



763 **FIG. A1. Input to the moist energy balance model.** The zonal-mean profile of (a) radiative forcing ( $R_f$ ),  
 764 (b) ocean heat uptake ( $G'$ ), and (c) the net radiative feedback ( $\lambda$ ) from 20 CMIP5 GCMs 126 – 150 years after  
 765 an abrupt quadrupling of  $\text{CO}_2$ . The grey lines represent each individual GCM and the colored lines denote the  
 766 multi-model mean.

## APPENDIX B

### Climatological Hadley Cell parameterization

In the main text, we introduce the Hadley Cell parameterization using the perturbation version of the MEBM. However, the mass transport of the Hadley Cell and thus the pattern of  $P' - E'$  depends to some extent on the climatological state via Eq. (10) and Eq. (11). To account for this, we use a climatological version of the MEBM to estimate the climatological state of each GCM. This is done by first calculating the net heating of the atmosphere  $Q_{\text{net}}(x)$ , which is the difference between the net downward energy flux at the TOA and the surface in preindustrial control simulations (see Appendix A). Because the northward column-integrated atmospheric energy transport  $F$  is assumed to be related to the meridional gradient in  $h$ , the climatological version of the MEBM (with a constant  $D$ ) is:

$$Q_{\text{net}}(x) = -\frac{p_s}{a^2 g} D \frac{d}{dx} \left[ (1-x^2) \frac{dh}{dx} \right]. \quad (\text{B1})$$

The MEBM climatological values of  $T(x)$  and  $q(x)$  (assuming relative humidity is fixed at 80%) can be found by minimizing the difference between the zonal-mean near-surface air temperature and  $Q_{\text{net}}$  from each GCM using Eq. B1. A similar procedure as described in Section 2 is then used to calculate  $\psi(x)$ ,  $H(x)$ , and  $P - E$  except that the poleward heat flux and moisture flux take the form of:

$$F_{\text{HC}}(x) = \psi(x)H(x), \quad (\text{B2})$$

and

$$F_{L,\text{HC}}(x) = \psi(x)L_v q(x), \quad (\text{B3})$$

respectively. Note that here  $D$  is unique to each GCM. For Section 3, the value of  $D$  is unique to each GCM and for Section 4, the value of  $D$  is  $1.05 \times 10^6 \text{ m}^2 \text{ s}^{-1}$  (i.e., the multi-model mean value). For Section 3, the climatological variables are unique to each GCM and for Section 4, the climatological variables are the multi-model mean patterns and made to be symmetric about the equator.

## APPENDIX C

### Diffusive energy transport scaling

791 The scaling in Eq. (17) was first derived by HS06 and can be found through the following  
 792 arguments. First, by assuming that moisture and temperature are diffused with the same diffusivity,  
 793 the ratio of the latent heat transport  $F_L$  to the sensible heat transport  $F_S$  will be the ratio of the  
 794 meridional gradient of  $L_v q$  to the meridional gradient of  $c_p T$ , meaning:

$$\frac{F_L}{F_S} = \frac{L_v}{c_p} \frac{dq}{dT}, \quad (\text{C1})$$

795 where

$$\frac{dq}{dT} = \frac{dq/dx}{dT/dx}. \quad (\text{C2})$$

796 Because the Clausius-Clapeyron equation states that:

$$\frac{dq}{dT} = \alpha q, \quad (\text{C3})$$

797 the fractional change in the moisture transport under warming can be approximated as:

$$\frac{F'_L}{F_L} \approx \frac{(\alpha q)'}{\alpha q} + \frac{F'_S}{F_S}, \quad (\text{C4})$$

798 which can be re-arranged to be:

$$\frac{F'_L}{F_L} \approx \left( \alpha - \frac{2}{T} \right) T' + \frac{F'_S}{F_S}. \quad (\text{C5})$$

799 Thus, the change in moisture transport under warming can be written as:

$$F'_L(x) \approx \beta F_L(x), \quad (\text{C6})$$

800 where

$$\beta = \left( \alpha - \frac{2}{T} \right) T' + \frac{dT'/dx}{dT/dx}. \quad (\text{C7})$$

801 Note that the fractional change in sensible heat transport is now written in terms of the gradient in  
 802 near-surface air temperature. Finally, the change in  $P - E$  under warming can be found by taking

803 the divergence of Eq. (C6) which, together with Eq. (C7), results in:

$$P' - E' = \underbrace{\beta(P - E)}_{\text{Term 1}} - \underbrace{\frac{1}{2\pi a^2} F_L \frac{d\beta}{dx}}_{\text{Term 2}}. \quad (\text{C8})$$

804 Here, Term 1 represents changes to the moisture content of the atmosphere under warming and  
805 Term 2 represents changes to the poleward moisture flux under warming. HS06 argue that the  
806 dependence of the saturation vapor pressure on  $T$  and the fractional change of sensible-heat  
807 transport in Eq. (C7) are small and can be ignored. They also argue that because the pattern  
808 of warming is relatively uniform, the second term on the right hand side of Eq. (C8), which  
809 represents changes to the transport of moisture, is close to zero. Removing these terms results  
810 in  $P' - E' = \beta(P - E) = \alpha T'(P - E)$ , which is exactly Eq. (4). Thus, for the extratropics, the  
811 HS06 scaling and the MEBM differ because of the pattern of temperature change  $T'$  and the  
812 climatological pattern of  $T$ , which determine the moisture content of the atmosphere and poleward  
813 moisture transport.

814 *Acknowledgments.* The authors thank Polina Khapikova for helpful comments on an earlier draft  
815 of this paper. Part of this research was supported by the University of Washington Mary Gates  
816 Endowment for Undergraduate Students. D.B.B was supported by an American Meteorologi-  
817 cal Society (AMS) Graduate Fellowship and the National Science Foundation (NSF) Graduate  
818 Research Fellowship Program (NSF Grant DGE1745301). N.S. was supported by NSF Grant  
819 AGS-1954663. G.H.R. was supported by NSF Grants AGS-2019647 and P2C2-2102829. K.C.A.  
820 was supported by NSF Grants AGS-1752796 and AGS-2019647, and an Alfred P. Sloan Research  
821 Fellowship (Grant FG-2020-13568). We thank the climate modeling groups for producing and  
822 making available their model output, which is accessible at the Earth System Grid Federation  
823 (ESGF) Portal (<https://esgf-node.llnl.gov/search/cmip5/>).

824 *Data availability statement.* The code and data for this study is available at  
825 <https://github.com/dbonan/energy-balance-models>.

## 826 **References**

- 827 Abernathey, R. P., I. Cerovecki, P. R. Holland, E. Newsom, M. Mazloff, and L. D. Talley, 2016:  
828 Water-mass transformation by sea ice in the upper branch of the Southern Ocean overturning.  
829 *Nature Geoscience*, **9 (8)**, 596–601.
- 830 Armour, K. C., N. Siler, A. Donohoe, and G. H. Roe, 2019: Meridional atmospheric heat transport  
831 constrained by energetics and mediated by large-scale diffusion. *Journal of Climate*, **32 (12)**,  
832 3655–3680.
- 833 Beer, E., and I. Eisenman, 2022: Revisiting the role of the water vapor and lapse rate feedbacks in  
834 the Arctic amplification of climate change. *Journal of Climate*, 1–33.
- 835 Bonan, D. B., K. Armour, G. Roe, N. Siler, and N. Feldl, 2018: Sources of uncertainty in the  
836 meridional pattern of climate change. *Geophysical Research Letters*, **45 (17)**, 9131–9140.
- 837 Boos, W. R., 2012: Thermodynamic scaling of the hydrological cycle of the Last Glacial Maximum.  
838 *Journal of Climate*, **25 (3)**, 992–1006.
- 839 Burls, N. J., and A. V. Fedorov, 2017: Wetter subtropics in a warmer world: Contrasting past  
840 and future hydrological cycles. *Proceedings of the National Academy of Sciences*, **114 (49)**,  
841 12 888–12 893.
- 842 Byrne, M. P., and P. A. O’Gorman, 2015: The response of precipitation minus evapotranspiration  
843 to climate warming: Why the “wet-get-wetter, dry-get-drier” scaling does not hold over land.  
844 *Journal of Climate*, **28 (20)**, 8078–8092.
- 845 Byrne, M. P., and T. Schneider, 2016a: Energetic constraints on the width of the intertropical  
846 convergence zone. *Journal of Climate*, **29 (13)**, 4709–4721.
- 847 Byrne, M. P., and T. Schneider, 2016b: Narrowing of the ITCZ in a warming climate: Physical  
848 mechanisms. *Geophysical Research Letters*, **43 (21)**, 11–350.
- 849 Carmichael, M. J., and Coauthors, 2016: A model–model and data–model comparison for the early  
850 Eocene hydrological cycle. *Climate of the Past*, **12 (2)**, 455–481.
- 851 Chang, E. K., Y. Guo, and X. Xia, 2012: CMIP5 multimodel ensemble projection of storm track  
852 change under global warming. *Journal of Geophysical Research: Atmospheres*, **117 (D23)**.

- 853 Chou, C., and J. D. Neelin, 2004: Mechanisms of global warming impacts on regional tropical  
854 precipitation. *Journal of climate*, **17 (13)**, 2688–2701.
- 855 Chou, C., T.-C. Wu, and P.-H. Tan, 2013: Changes in gross moist stability in the tropics under  
856 global warming. *Climate dynamics*, **41 (9)**, 2481–2496.
- 857 Dai, A., and K. E. Trenberth, 2002: Estimates of freshwater discharge from continents: Latitudinal  
858 and seasonal variations. *Journal of hydrometeorology*, **3 (6)**, 660–687.
- 859 de Boyer Montégut, C., J. Mignot, A. Lazar, and S. Cravatte, 2007: Control of salinity on the  
860 mixed layer depth in the world ocean: 1. General description. *Journal of Geophysical Research:  
861 Oceans*, **112 (C6)**.
- 862 Emori, S., and S. Brown, 2005: Dynamic and thermodynamic changes in mean and extreme  
863 precipitation under changed climate. *Geophysical Research Letters*, **32 (17)**.
- 864 Feldl, N., and S. Bordoni, 2016: Characterizing the Hadley circulation response through regional  
865 climate feedbacks. *Journal of Climate*, **29 (2)**, 613–622.
- 866 Feldl, N., S. Po-Chedley, H. K. Singh, S. Hay, and P. J. Kushner, 2020: Sea ice and atmospheric  
867 circulation shape the high-latitude lapse rate feedback. *NPJ climate and atmospheric science*,  
868 **3 (1)**, 1–9.
- 869 Field, C. B., and V. R. Barros, 2014: *Climate change 2014—Impacts, adaptation and vulnerability:  
870 Regional aspects*. Cambridge University Press.
- 871 Flannery, B. P., 1984: Energy balance models incorporating transport of thermal and latent energy.  
872 *Journal of the Atmospheric Sciences*, **41 (3)**, 414–421.
- 873 Frierson, D. M., 2008: Midlatitude static stability in simple and comprehensive general circulation  
874 models. *Journal of the atmospheric sciences*, **65 (3)**, 1049–1062.
- 875 Frierson, D. M., I. M. Held, and P. Zurita-Gotor, 2007: A gray-radiation aquaplanet moist GCM.  
876 Part II: Energy transports in altered climates. *Journal of the Atmospheric Sciences*, **64 (5)**,  
877 1680–1693.

878 Groeskamp, S., S. M. Griffies, D. Iudicone, R. Marsh, A. G. Nurser, and J. D. Zika, 2019: The  
879 water mass transformation framework for ocean physics and biogeochemistry. *Annual review of*  
880 *marine science*, **11**, 271–305.

881 Held, I. M., 2001: The partitioning of the poleward energy transport between the tropical ocean  
882 and atmosphere. *Journal of the Atmospheric Sciences*, **58 (8)**, 943–948.

883 Held, I. M., and B. J. Soden, 2006: Robust responses of the hydrological cycle to global warming.  
884 *Journal of climate*, **19 (21)**, 5686–5699.

885 Hill, S. A., N. J. Burls, A. Fedorov, and T. M. Merlis, 2022: Symmetric and antisymmetric  
886 components of polar-amplified warming. *Journal of Climate*, 1–49.

887 Hwang, Y.-T., and D. M. Frierson, 2010: Increasing atmospheric poleward energy transport with  
888 global warming. *Geophysical Research Letters*, **37 (24)**.

889 Kang, S. M., and J. Lu, 2012: Expansion of the Hadley cell under global warming: Winter versus  
890 summer. *Journal of Climate*, **25 (24)**, 8387–8393.

891 Large, W. G., and A. G. Nurser, 2001: Ocean surface water mass transformation. *International*  
892 *Geophysics*, Vol. 77, Elsevier, 317–336.

893 Lau, W. K., and K.-M. Kim, 2015: Robust Hadley circulation changes and increasing global  
894 dryness due to CO<sub>2</sub> warming from CMIP5 model projections. *Proceedings of the National*  
895 *Academy of Sciences*, **112 (12)**, 3630–3635.

896 Liu, M., G. Vecchi, B. Soden, W. Yang, and B. Zhang, 2021: Enhanced hydrological cycle  
897 increases ocean heat uptake and moderates transient climate change. *Nature Climate Change*,  
898 **11 (10)**, 848–853.

899 Lu, J., G. Chen, and D. M. Frierson, 2010: The position of the midlatitude storm track and eddy-  
900 driven westerlies in aquaplanet AGCMs. *Journal of Atmospheric Sciences*, **67 (12)**, 3984–4000.

901 Lu, J., G. A. Vecchi, and T. Reichler, 2007: Expansion of the Hadley cell under global warming.  
902 *Geophysical Research Letters*, **34 (6)**.

- 903 Lutsko, N. J., J. T. Seeley, and D. W. Keith, 2020: Estimating Impacts and Trade-offs in Solar  
904 Geoengineering Scenarios With a Moist Energy Balance Model. *Geophysical Research Letters*,  
905 **47 (9)**, e2020GL087290.
- 906 Marshall, J., J. R. Scott, K. C. Armour, J.-M. Campin, M. Kelley, and A. Romanou, 2015: The  
907 ocean's role in the transient response of climate to abrupt greenhouse gas forcing. *Climate*  
908 *Dynamics*, **44 (7)**, 2287–2299.
- 909 Mbengue, C., and T. Schneider, 2013: Storm track shifts under climate change: What can be  
910 learned from large-scale dry dynamics. *Journal of Climate*, **26 (24)**, 9923–9930.
- 911 Mbengue, C., and T. Schneider, 2017: Storm-track shifts under climate change: Toward a mecha-  
912 nistic understanding using baroclinic mean available potential energy. *Journal of the Atmospheric*  
913 *Sciences*, **74 (1)**, 93–110.
- 914 Mbengue, C., and T. Schneider, 2018: Linking Hadley circulation and storm tracks in a conceptual  
915 model of the atmospheric energy balance. *Journal of the Atmospheric Sciences*, **75 (3)**, 841–856.
- 916 Merlis, T. M., and M. Henry, 2018: Simple estimates of polar amplification in moist diffusive  
917 energy balance models. *Journal of Climate*, **31 (15)**, 5811–5824.
- 918 Mitchell, J., C. Wilson, and W. Cunnington, 1987: On CO<sub>2</sub> climate sensitivity and model depen-  
919 dence of results. *Quarterly Journal of the Royal Meteorological Society*, **113 (475)**, 293–322.
- 920 Mooring, T. A., and T. A. Shaw, 2020: Atmospheric diffusivity: A new energetic framework for  
921 understanding the midlatitude circulation response to climate change. *Journal of Geophysical*  
922 *Research: Atmospheres*, **125 (1)**, e2019JD031206.
- 923 O’Gorman, P. A., and T. Schneider, 2008: The hydrological cycle over a wide range of climates  
924 simulated with an idealized GCM. *Journal of Climate*, **21 (15)**, 3815–3832.
- 925 Peterson, H. G., and W. R. Boos, 2020: Feedbacks and eddy diffusivity in an energy balance model  
926 of tropical rainfall shifts. *npj Climate and Atmospheric Science*, **3 (1)**, 1–9.
- 927 Pithan, F., and T. Mauritsen, 2014: Arctic amplification dominated by temperature feedbacks in  
928 contemporary climate models. *Nature geoscience*, **7 (3)**, 181–184.

- 929 Prein, A. F., and A. G. Pendergrass, 2019: Can we constrain uncertainty in hydrologic cycle  
930 projections? *Geophysical Research Letters*, **46** (7), 3911–3916.
- 931 Roe, G. H., N. Feldl, K. C. Armour, Y.-T. Hwang, and D. M. Frierson, 2015: The remote impacts  
932 of climate feedbacks on regional climate predictability. *Nature Geoscience*, **8** (2), 135–139.
- 933 Russotto, R. D., and M. Biasutti, 2020: Polar amplification as an inherent response of a circulating  
934 atmosphere: results from the TRACMIP aquaplanets. *Geophysical Research Letters*, **47** (6),  
935 e2019GL086771.
- 936 Scheff, J., and D. Frierson, 2012: Twenty-first-century multimodel subtropical precipitation de-  
937 clines are mostly midlatitude shifts. *Journal of Climate*, **25** (12), 4330–4347.
- 938 Schmitt, R. W., P. S. Bogden, and C. E. Dorman, 1989: Evaporation minus precipitation and  
939 density fluxes for the North Atlantic. *Journal of Physical Oceanography*, **19** (9), 1208–1221.
- 940 Seager, R., N. Naik, and G. A. Vecchi, 2010: Thermodynamic and dynamic mechanisms for  
941 large-scale changes in the hydrological cycle in response to global warming. *Journal of Climate*,  
942 **23** (17), 4651–4668.
- 943 Seager, R., and G. A. Vecchi, 2010: Greenhouse warming and the 21st century hydroclimate  
944 of southwestern North America. *Proceedings of the National Academy of Sciences*, **107** (50),  
945 21 277–21 282.
- 946 Shaw, T. A., and A. Voigt, 2016: What can moist thermodynamics tell us about circulation shifts  
947 in response to uniform warming? *Geophysical Research Letters*, **43** (9), 4566–4575.
- 948 Siler, N., G. H. Roe, and K. C. Armour, 2018: Insights into the zonal-mean response of the  
949 hydrologic cycle to global warming from a diffusive energy balance model. *Journal of Climate*,  
950 **31** (18), 7481–7493.
- 951 Siler, N., G. H. Roe, K. C. Armour, and N. Feldl, 2019: Revisiting the surface-energy-flux  
952 perspective on the sensitivity of global precipitation to climate change. *Climate Dynamics*,  
953 **52** (7), 3983–3995.
- 954 Su, H., J. H. Jiang, C. Zhai, T. J. Shen, J. D. Neelin, G. L. Stephens, and Y. L. Yung, 2014:  
955 Weakening and strengthening structures in the Hadley Circulation change under global warming

- 956 and implications for cloud response and climate sensitivity. *Journal of Geophysical Research:*  
957 *Atmospheres*, **119** (10), 5787–5805.
- 958 Su, H., C. Zhai, J. H. Jiang, L. Wu, J. D. Neelin, and Y. L. Yung, 2019: A dichotomy between  
959 model responses of tropical ascent and descent to surface warming. *npj Climate and Atmospheric*  
960 *Science*, **2** (1), 1–8.
- 961 Taylor, K. E., R. J. Stouffer, and G. A. Meehl, 2012: An overview of CMIP5 and the experiment  
962 design. *Bulletin of the American Meteorological Society*, **93** (4), 485–498.
- 963 Winguth, A., C. Shellito, C. Shields, and C. Winguth, 2010: Climate response at the Paleocene–  
964 Eocene Thermal Maximum to greenhouse gas forcing—A model study with CCSM3. *Journal*  
965 *of Climate*, **23** (10), 2562–2584.